

CFD analysis of intra and inter fuel assembly mixing

Ulrich Bieder, Clarisse Genrault

▶ **To cite this version:**

Ulrich Bieder, Clarisse Genrault. CFD analysis of intra and inter fuel assembly mixing. Annals of Nuclear Energy, 2020, 135, pp.106977. 10.1016/j.anucene.2019.106977 . cea-02529690

HAL Id: cea-02529690

https://cea.hal.science/cea-02529690

Submitted on 20 Jul 2022

HAL is a multi-disciplinary open access archive for the deposit and dissemination of scientific research documents, whether they are published or not. The documents may come from teaching and research institutions in France or abroad, or from public or private research centers.

L'archive ouverte pluridisciplinaire **HAL**, est destinée au dépôt et à la diffusion de documents scientifiques de niveau recherche, publiés ou non, émanant des établissements d'enseignement et de recherche français ou étrangers, des laboratoires publics ou privés.



Distributed under a Creative Commons Attribution - NonCommercial| 4.0 International License

Version of Record: https://www.sciencedirect.com/science/article/pii/S0306454919304724
Manuscript_165c60358a4f88f07929ebbb8ae2acec

CFD analysis of intra and inter fuel assembly mixing

Ulrich Bieder, Clarisse Genrault

DEN-STMF, CEA, Université Paris-Saclay, 91191 Gif-sur-Yvette, France

1. INTRODUCTION

The reactor core of a PWR (Pressurized Water Reactor) is assembled from arrays of nuclear fuel bundles, which in turn are typically composed by 15×15 or 17×17 fuel rods. Support and mixing grids are positioned within the assembly at specific axial distances to maintain the lateral spacing of fuel rods. Since turbulent, force convection dominates the transport of the thermal energy from the surfaces of the fuel rods to the bulk of the fluid, mixing vanes are placed on the top edges of the mixing grid lattice in order to enhance turbulence and thus heat transfer. The cooling water flows mainly in the direction parallel to the rods. Due to the mixing vanes, cross flow occurs in planes orthonormal to the axial direction.

The temperature distribution in nuclear reactor fuel assemblies is a function of the mixing efficiency of the mixing grid, the turbulence level of the flow and the cross flow velocity. The onset of nucleate boiling is expected far downstream of the mixing grids, where both turbulence level and cross flow velocities are low. Hence, it is important not only to focus CFD applications on the flow close to the mixing grid, but also on the flow further downstream of the grid. Furthermore, evidence was found that temperature fluctuations could be induced by cross flow within a fuel assembly (*intra-assembly* mixing) and between neighboring fuel assemblies (*inter-assembly* mixing). Such temperature fluctuations can potentially damage the fuel rod cladding, especially in the upper part of the core where the heat flux density is small.

Karoutas et al. (1995) realized one of the first CFD simulations of turbulent flow in a fuel bundle with mixing vanes by using Reynolds Averaged Navier Stokes Equations (RANS). However, only half of a single sub channel was simulated using symmetry boundary conditions. Navarro and Santos (2011) improved these results using a computational domain of a 5×5 rods. Such 5×5 rod bundle domains have been extensively analyzed in various studies. Exemplified cited is the MATIS_H experiment (Smith et al., 2013) that was analyzed among others by Agbodemegbe et al. (2015), Capone et al. (2013), Mikuž and Tiselj (2017) and Rashkovan et al. (2014). Bieder et al. (2014) and Muller et al (2018) analyzed the AGATE experiments and the NESTOR experiments were studied by Kang and Hassan (2016). Other 5x5 experiments were investigated for example by Conner et al. (2013), Holloway et al. (2008), Gandhir and Hassan (2011) as well as Nguyen and Hassan (2017).

Lee and Choi (2007) showed the effect of different positions and orientations of mixing vanes on thermo-hydraulic performances. A Reynolds Stress Transport Model (RSTM) was used to see the effects of secondary flow. Conner et al. (2010) compared CFD simulations with experiments and obtained satisfactory prediction of cross flow velocity and heat transfer. According to Conner et al. (2010), Westinghouse has tested and validated in extensive research the applicability of turbulence models to simulate fuel rod bundles. The renormalization group (RNG) k–ε model had been found to produce the closest agreement with available experimental data. Gandhir and Hassan (2011) have analyzed the flow in a 5×5 rod bundle with mixing grid up to an axial length of 30 hydraulic diameters by using k-ω SST and realizable k-ε model. The magnitude of the calculated cross flow velocity downstream of the grid differs between the two models approximately by a factor of four.

For the complete axial distance between two mixing grids, Ylönen (2013) has reported high quality experimental data for a 4x4 rod bundle. This data has also been analyzed with CFD calculations by using RSTM. He concluded that reasonable qualitative agreement between experiment and simulation was achieved with moderate modelling effort.

© 2019 published by Elsevier. This manuscript is made available under the CC BY NC user license
https://creativecommons.org/licenses/by-nc/4.0/

Ikeno et al. (2006) used Large Eddy Simulations (LES) to model cross flow and its decay downstream of a mixing grid. They conclude that the computational results reasonably reproduced experimental results for the drag coefficient (difference of a factor two) and the decay rate of swirling flow. Delafontaine and Ricciardi (2012) used LES to predict the fluctuating pressure forces on a single tube in a bi-periodic 2×2 rod bundle with mixing grid.

Due to the important increase of computational power in recent years, first CFD analysis of full size fuel assemblies have been published. Li and Gao (2014) simulated a 17×17 rod bundle with a single mixing grid. However, only a short axial length of 22 mm was analyzed. Yan et al. (2014) have analyzed by CFD the influence of the mixing grid outer straps (protective tabs) on the flow within adjacent assemblies. One full assembly of 17×17 rods was subdivided into four sub-assemblies, each representing one quarter of the full assembly. These four quarters were regathered to model the water gaps. The CFD results were compared to results of sub channel codes.

Mikuž and Roelofs (2018) analyzed mixing phenomena in a heated PWR fuel assembly of 15×15 rods with split type mixing grids. They assumed all rods being similar and used a so-called *low-resolution approach* with porous media and momentum models to mimic the effect of spacers. They analyzed a complete fuel assembly of 5.2 m length (4.8 m length of fuel rods) including the effects of 10 mixing grids. The heated length of the fuel rods was 4.2 m. At the upper limit of the heated zone, Mikuž and Roelofs (2018) detected a slightly colder diagonally arranged zone in the fuel assembly.

To the knowledge of the authors, the flow within and between full cross-section fuel assemblies with generic but realistic mixing grids has not been analyzed and published with fully resolved RANS and LES simulations. The here presented work tries in a first attempt to close this gap by using high performance computing (HPC). The analyzed assembly consists of a bundle of 17×17 rods including fuel rods, control rod guide tubes and a mixing grid. The axial length of the analyzed domain spans approximately the distance between two consecutive mixing grids. *Intra-assembly* flow is analyzed by modelling one single assembly; *inter-assembly* flow is analyzed by modelling a bundle of 2×2 fuel assemblies. Only hydraulic effects of the mixing grids on the behavior of the flow are analyzed yet; power input and heat transfer will be considered in subsequent studies.

2. THE GENERIC FUEL ASSEMBLY WITH MIXING GRID

The calculation domain comprises a part of a PWR fuel assembly (FA) of 17×17 fuel rods including a mixing grid. Mixing grids (also called spacer grids) maintain the lateral spacing between fuel rods and support the fuel rods at intervals along their length. The mixing grid consists of an *egg-crate* arrangement of interlocking straps. The straps contain spring fingers and dimples for fuel rod support as well as coolant mixing vanes (Weihermiller and Allison, 1979). Guide taps on the outer straps assure the unhindered axial movement of the fuel assembly during charge and discharge of the reactor core. The representation of the fuel assembly and the mixing grid given in Fig.1 served as basis for the fuel assembly model.

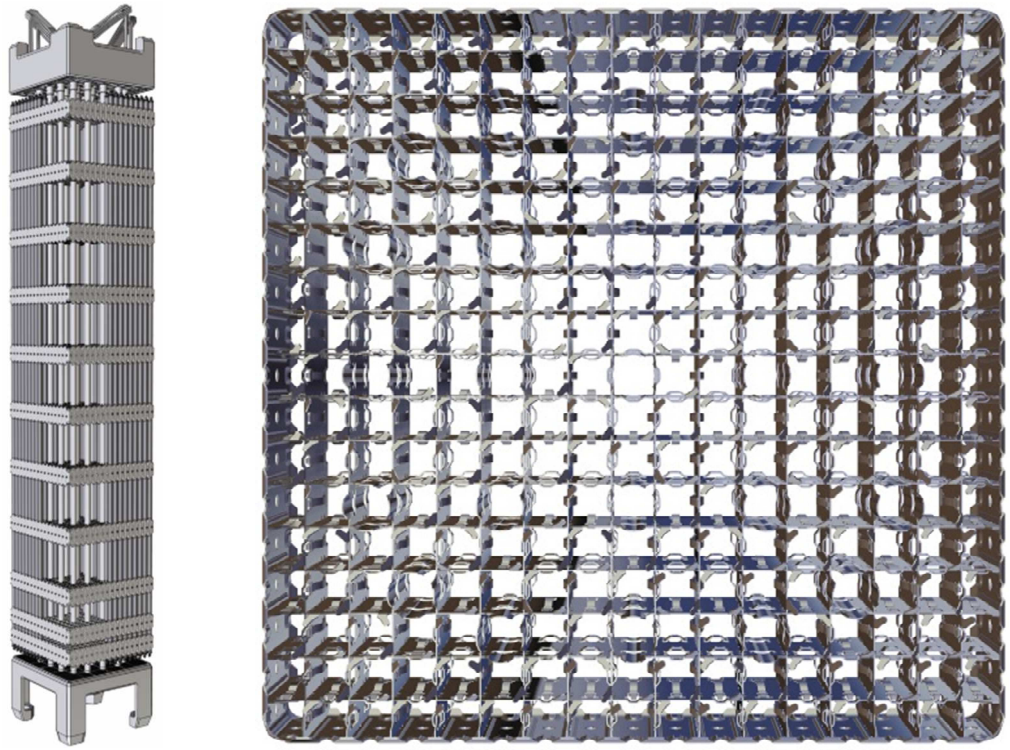


Fig.1 Fuel assembly and mixing grid that have inspired the geometry of the generic FA model

This figure, whose precise origin can no more be evaluated by the authors, was found on the internet in 2010. Especially the arrangement of springs, dimples, mixing vanes and protective tabs was deduced from this figure. The resulting CAD model of the generic mixing grid is shown in Fig.2. The CAD model was developed in SALOME[1]; it is parametrized by PYTHON scripts in order to have the possibility to modify easily the geometry of the mixing grid for further studies.

Two numbers define the location of rods and guide tubes in the assembly; the first one defines the number of the column, the second the number of the row. As defined in Fig.2, the rows follow the x-direction and the columns follow the y-direction (location of a rod n° = column : row).

[1] https://salome-platform.org/

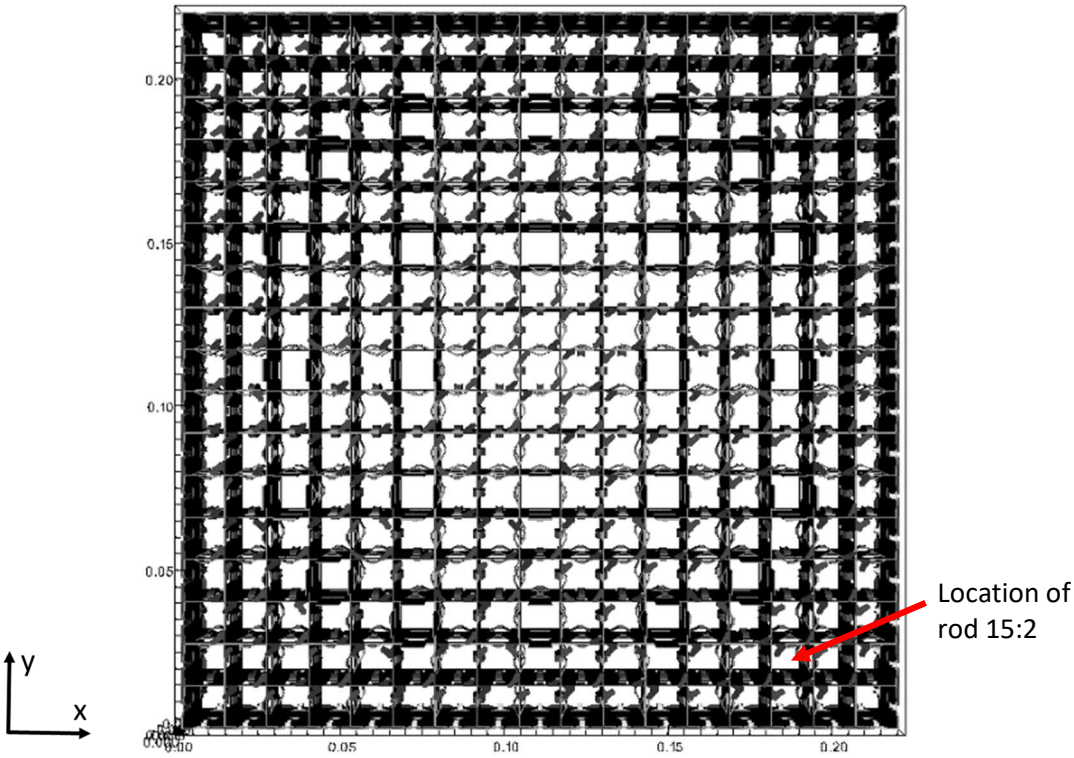


Fig.2 Top view of the generic mixing grid and an example for the numbering of rods and guide tubes

A zoom on the CAD-model of fuel rods, guide tube, springs, dimples, lattice strap and protective tabs is given in Fig.3. Guide tubes have a larger diameter than fuel rods. They are not fasten by springs and dimples but by guide thimbles that are joined to the straps.

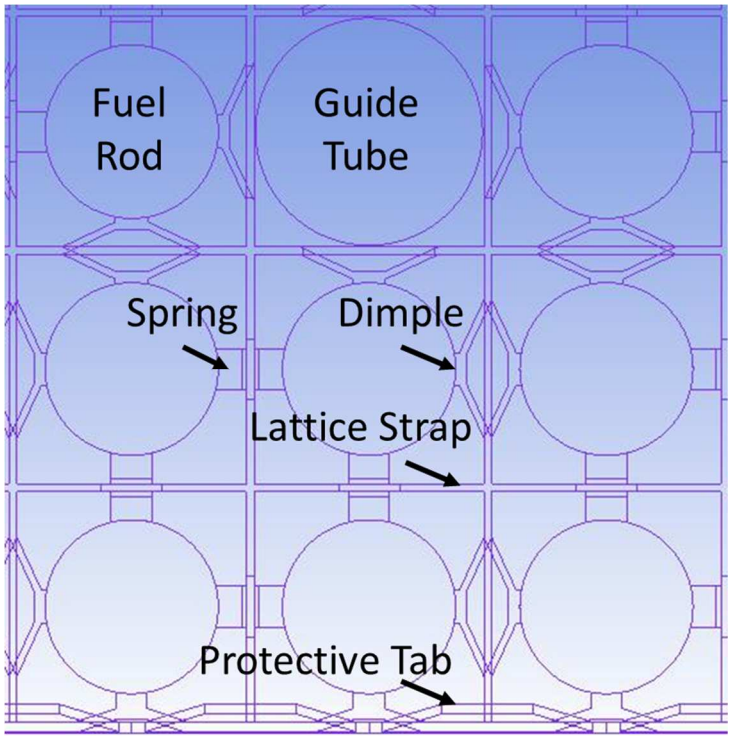


Fig.3 Zoom on fuel rods, guide tubes, grid strap, springs and dimples (top view)

The protective tabs are located on the outer lattice straps, which have a slightly higher width than the inner straps (Weihermiller and Allison, 1979). The geometry of the springs is simplified; they

are not modelled as bands. The tangential contact between dimple and fuel rod was avoided by increasing their contact zone.

Fig.4 shows a generic form of split type mixing vanes with a triangular central hole. Drop wise holes as used by Delafontaine (2018) and Capone (2012) are used for the calculations presented here. The angle between grid strap and vane is 33°. The mixing vanes are arranged on the straps to initiate diagonal cross flow in order to increase the flow mixing between sub-channels. Mixing vanes are absent in the sub-channels around the control rod guide tubes. Weld nuggets (Capone, 2012) are not modeled.

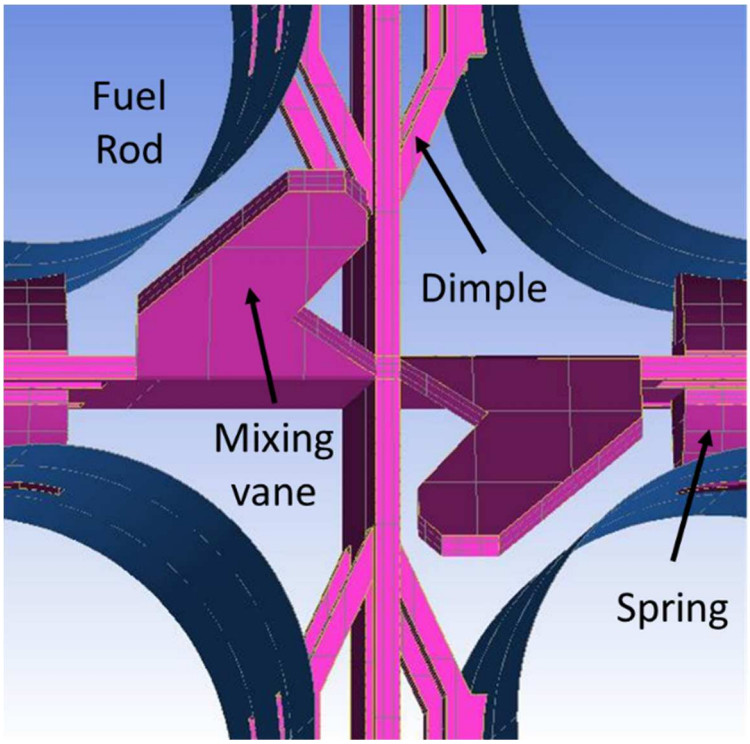


Fig.4 Zoom on fuel rods, guide tubes, springs dimples and mixing vanes (top view)

Protective tabs are located at the lateral grid straps, all oriented inside the mixing grid. A summary of the geometry of the FA is given below:

• Rod diameter	9.5	mm
• Rod-to-rod pitch	13.0	mm
• Rod-to-rod gap	3.5	mm
• Hydraulic diameter of a sub channel	13.15	mm
• Pitch/rod ratio	1.368	
• Control rod guide tube diameter	11.64	mm
• Side to side distance of the FA	224	mm
• Height of mixing grid	41	mm
• Gap between 2 adjacent FAs (water gap)	2	mm
• Distance between successive mixing grids	340	mm

3. THE NUMERICAL MODEL

The TrioCFD code (Angeli et al., 2015) is used for all calculations presented here. Turbulence is treated either by RANS equations with the linear eddy viscosity k-ε model or by LES.

3.1 UNSTEADY NAVIER-STOKES EQUATIONS

The fluid is assumed Newtonian and incompressible. As only isothermal flow is discussed in this work, buoyancy effects are not taken into account. The instantaneous velocity *u* of such a fluid can be expressed by the equation of mass conservation Eq.1 and momentum conservation Eq.2 (Pope, 2000). Einstein's matrix notation is used.

$$\frac{\partial u_j}{\partial x_j} = 0 \tag{1}$$

$$\frac{\partial u_i}{\partial t} + \frac{\partial (u_i u_j)}{\partial x_j} = -\frac{1}{\rho}\frac{\partial p}{\partial x_i} + \frac{\partial}{\partial x_j}\left[\nu_{eff}\left(\frac{\partial u_i}{\partial x_j} + \frac{\partial u_j}{\partial x_i}\right)\right] + \frac{S_{M,i}}{\rho} \tag{2}$$

For laminar flow, the effective viscosity ν_{eff} is the kinematic viscosity ν of the fluid. S_M is a momentum source term.

3.2 TURBULENCE MODELLING

The Reynolds number of the flow in the analyzed fuel assembly is about 500000. Thus, turbulence is modelled for closing of the Navier-Stokes equations. Two physically different models were selected: Unsteady Reynolds averaged Navier-Stokes equations (U-RANS) and filtered Navier-Stokes equations for large eddy simulations (LES).

3.2.1 Reynolds averaged Navier-Stokes equations

In Reynolds-averaging turbulence modelling, an averaging operation denoted by $\bar{}$ is applied to the instantaneous velocity in Eqs. (1, 2). The non-linearity of the Navier-Stokes equations gives rise to Reynolds stress terms that are modeled by turbulence models. Most turbulence models for industrial applications are based on Boussinesq's concept of eddy-viscosity, which assumes that the Reynolds stresses are aligned with the main strain rates:

$$\tau_{ij} \equiv -\overline{u_i' u_j'} = \nu_{RANS}\left(\frac{\partial \overline{u_i}}{\partial x_j} + \frac{\partial \overline{u_j}}{\partial x_i}\right) - \frac{2}{3\cdot\rho} k \delta_{ij} \tag{3}$$

The Reynolds averaging approach leads to the Reynolds averaged mass conservation equation and the Navier-Stokes equations. For the RANS approach, Eqs. (1, 2) are written for the Reynolds averaged velocity $\overline{u_i}$ and $\nu_{eff} = \nu + \nu_t$. In the study presented here, the turbulent viscosity ν_t is calculated from the well-known k-ε model by using the following formulation (Pope, 2000):

$$\upsilon_t = c_\mu \frac{k}{\varepsilon} \tag{4}$$

$$\frac{\partial k}{\partial t} + \frac{\partial (\overline{u_j} k)}{\partial x_j} = \frac{\partial}{\partial x_j}\left[\left(\nu + \frac{\nu_t}{\sigma_k}\right)\frac{\partial k}{\partial x_j}\right] - \varepsilon + P \tag{5}$$

$$\frac{\partial \varepsilon}{\partial t} + \frac{\partial (\overline{u_j} \varepsilon)}{\partial x_j} = \frac{\partial}{\partial x_j}\left[\left(\nu + \frac{\nu_t}{\sigma_\varepsilon}\right)\frac{\partial \varepsilon}{\partial x_j}\right] + C_{\varepsilon 1} P \frac{\varepsilon}{k} - C_{\varepsilon 2}\frac{\varepsilon^2}{k} \tag{6}$$

$$P = -\overline{u_i' u_j'}\frac{\partial U_i}{\partial x_j} \tag{7}$$

The Reynolds stresses $\overline{u_i' u_j'}$ are calculated from Eq.3. The following empirical coefficients are used: c_μ=0.09, σ_k=1, σ_ε=1.3, $C_{\varepsilon 1}$=1.44, $C_{\varepsilon 2}$=1.92.

3.2.2 Filtered Navier-Stokes equations

In large eddy simulations (LES), a filtering operation denoted by ~ is applied to the instantaneous velocity of Eqs. (1, 2). The appearing sub-grid-scale stress tensor τ_{ij} is calculated using an analogy to the Boussinesq eddy viscosity concept:

$$\tau_{ij} \equiv \left(\widetilde{u_i}\widetilde{u_j} - \widetilde{u_i}\cdot\widetilde{u_j}\right) = \nu_{SGS}\left(\frac{\partial\widetilde{u_i}}{\partial x_j} + \frac{\partial\widetilde{u_j}}{\partial x_i}\right) + \frac{1}{3}\frac{k}{\rho}\delta_{ij} \tag{8}$$

Then, Eqs. (1, 2) are written for the filtered velocity $\widetilde{u_i}$ and $\nu_{eff} = \nu + \nu_{SGS}$. The wall adaptive local eddy-viscosity (WALE) model is applied (Nicoud and Ducros, 1996) to calculate the sub-grid-scale viscosity ν_{SGS} according to the following equations (C_w=0.5):

$$\nu_{SGS} = (C_w\overline{\Delta})^2 \frac{\left(s_{ij}^d \cdot s_{ij}^d\right)^{3/2}}{\left(S_{ij}\cdot S_{ij}\right)^{5/2} + \left(S_{ij}\cdot S_{ij}\right)^{5/4} + 10^{-6}} \tag{9}$$

with

$$S_{ij} = \frac{1}{2}\left(\frac{\partial\widetilde{u_i}}{\partial x_j} + \frac{\partial\widetilde{u_j}}{\partial x_i}\right) \qquad \text{and} \qquad s_{ij}^d = \frac{1}{2}\left(\left(\frac{\partial\widetilde{u_i}}{\partial x_j}\right)^2 + \left(\frac{\partial\widetilde{u_j}}{\partial x_i}\right)^2\right) - \frac{1}{3}\left(\frac{\partial\widetilde{u_i}}{\partial x_i}\right)^2 \cdot \delta_{ii} \tag{10}$$

3.3 NUMERICAL SOLUTION OF THE CONSERVATION EQUATIONS

3.3.1 Discretization method

TrioCFD (Angeli et al, 2015) uses a finite volume based finite element approach on tetrahedral cells to integrate in conservative form all conservation equations over the control volumes belonging to the calculation domain. As in the classical Crouzeix–Raviart element, both vector and scalar quantities are located in the centers of the faces (Angeli et al., 2018). The pressure, however, is located in the vertices and at the center of gravity of a tetrahedral element, as shown for the 2D case by Höhne et al. (2006). This discretization leads to very good pressure/velocity coupling and has a very dense divergence free basis. Along this staggered mesh arrangement, the unknowns, i.e. the vector and scalar values, are expressed using non-conforming linear shape-functions (P1-non-conforming). The shape function for the pressure is constant for the center of the element (P0) and linear for the vertices (P1). Angeli et al. (2018) give more information on the discretization method.

3.3.2 Solution method

For the two types of turbulence modelling approaches, different solution methods are used. For RANS calculation, the 1st order Euler backward time marching scheme was used to solve the momentum equations. A fully implicit velocity projection method assures the mass conservation. Guermond and Quartapelle (1998) have demonstrated the stability of this scheme. For LES, the explicit 2nd order Adams-Bashforth time marching scheme was used to solve the momentum equations. The SOLA pressure projection method of Hirt et al. (1975) assures the mass conservation. The convergence thresholds have been set to 10^{-6} for all calculations presented here.

3.3.3 Boundary and initial conditions

Dirichlet boundary conditions were used at inflow faces. Fully developed turbulent flow in a bare rod bundle without mixing grids is assumed at the inlet (Bieder et al. 2014). In order to create the corresponding velocity profiles, a periodic sub-domain is extruded from the inflow faces. Periodicity is applied on this sub-domain as boundary condition in axial direction. The flow is initialized with the desired spatially constant mean axial velocity (5.35m/s). Then, the flow develops temporally in the periodic domain during a transient. A momentum source term assures a constant mean axial mass flow rate. After transition to turbulence, the transient was continued until both the temporal mean values and the RMS of the velocity have converged. Temporally constant profiles of velocity, k and ε are used for RANS calculations, the instantaneous velocity of the periodic domain is imposed at each time step for LES (Bieder et al. 2014). Neumann conditions with an imposed

pressure are applied at outflow faces. Standard wall functions are used to model momentum exchange between walls and fluid. In fact, Reichardt's general wall law (Eq. (11) with κ=0.415) is used, which spans with one correlation viscous-, buffer- and turbulent sub-layer (Reichardt, 1951).

$$u^+ = \frac{1}{\kappa}\ln(1+\kappa y^+) + 7.8\left[1 - e^{\left(-\frac{y^+}{11}\right)} - \frac{y^+}{11}e^{\left(-\frac{y^+}{3}\right)}\right]. \quad (11)$$

A slip wall boundary condition (symmetry) is applied at the boundaries that surround laterally the rod bundle in order to mimic free flow conditions in the water gaps between adjacent FAs.

3.3.4 Parallelization

The presented CFD calculations have been carried out by exploiting the parallel calculation capabilities of the code. Using METIS libraries, each domain is decomposed into several overlapping sub-domains; all sub-domains were equally distributed among different processor cores, which, by using message passing interface libraries (MPI), communicate mutually only when data transfer is needed.

3.3.5 Summary of the numerical scheme

For the two types of turbulence modelling approaches, slightly different numerical schemes are used. For RANS calculation, a finite-element based 2nd order upwind scheme is used to discretise the convection term (called ef_stab). Ducros et al. (2010) give detailed information on this scheme. The complete numerical scheme for RANS calculations is summarized in Table 1

Table 1: RANS numerical scheme

Mesh	Tetrahedral mesh	
Time scheme	Euler backward	1rd order implicit
Spatial Discretisation	Convection	2nd order upwind
	Diffusion	2nd order centred
	Pressure solver	Conjugated gradient with SSOR preconditioning
Turbulence	U-RANS	k-ε
	Wall law	Law of Reichhardt

For LES, the convection term is discretized by a 2nd order centered scheme developed by Kuzmin and Turek (2004) for scalar transport. Fortin (2006) has extended this scheme to momentum transport. Additional information on the LES numerical scheme is summarized in Table 2.

Table 2: LES numerical scheme

Mesh	Tetrahedral mesh	
Time scheme	Adams-Bashforth	2nd order explicit
Spatial Discretisation	Convection	2nd order centred
	Diffusion	2nd order centred
	Pressure solver	Conjugated gradient with SSOR preconditioning
Turbulence	LES	WALE
	Wall law	Law of Reichhardt

3.4 THE MESHING

The CAD model was built in SALOME and was transferred in STEP format to the commercial mesh generator ICEMCFD®. A pure tetrahedral meshing was created around the mixing grid in the region called *Meshed Zone* that has an axial extension of 43 mm (see Fig.5). Then, the surface mesh of the axial boundaries of the *Meshed Zone*, which is represented by triangles, was extruded uniformly in z-direction, more precisely -30 mm in upstream direction and +300 mm in downstream direction. Each created prismatic cell has an axial length of 3 mm. Each prism is then divided into 3 tetrahedrons. The resulting calculation domain of one assembly of 17×17 rods is shown in Fig.5 including the inlet and outlet plane.

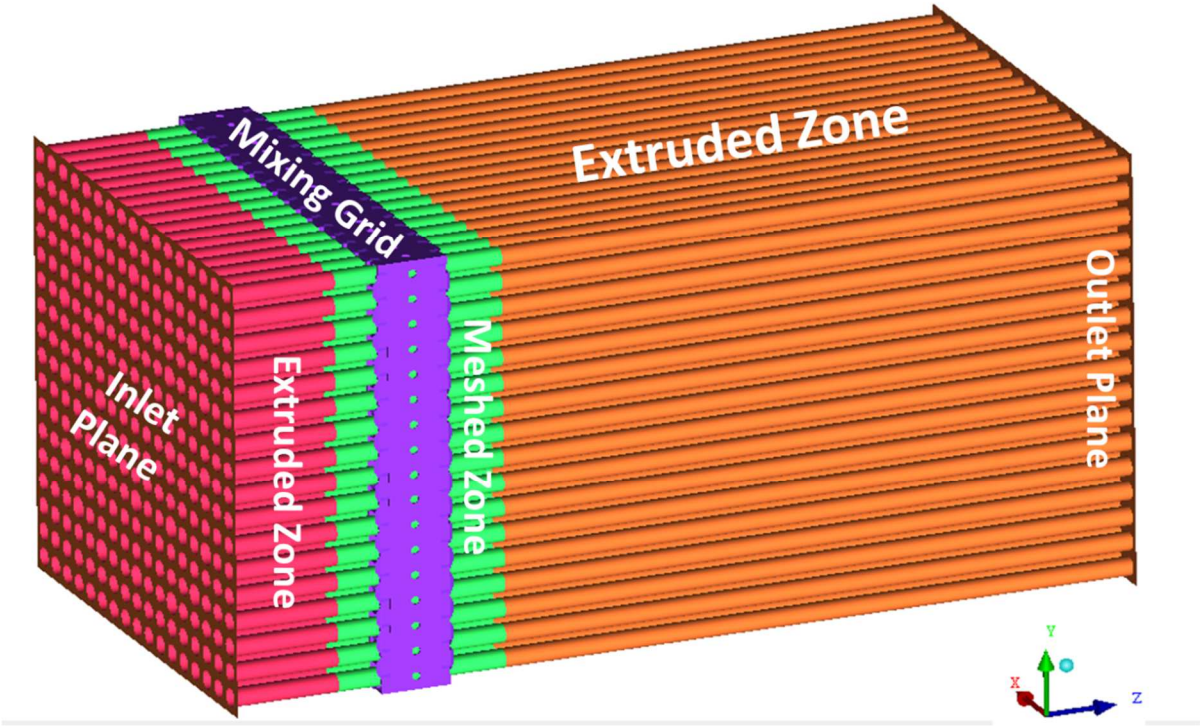


Fig.5 Calculation domain of the fuel assembly with mixing grid, meshed and extrudes zones as well as inlet and outlet planes.

Various tests concerning the meshing method (Delaunay, octree, advancing front, tgrid) and local mesh refinement near walls were performed. For the same number of tetrahedrons, these tests lead to the conclusion that the best performance concerning the resolution time of one time step is achieved with the Delaunay meshing method and using a homogeneous mesh size in the whole calculation domain (no local mesh refinement). Two meshes were finally retained, one for LES with a reference size of 1 mm and 50 million tetrahedral cells in the *Meshed Zone* and one for RANS calculations with a reference size of 5 mm and 20 million tetrahedrons in the *Meshed Zone*. Fig.6 shows the meshing of the control volumes for mass conservation inside the mixing grid with the presence of the grid strap, a vane and a dimple. The meshing downstream of the mixing grid with fuel rods and a guide tube (control volumes for mass conservation) is given in Fig.7. Prismatic cells near fuel rods, guide tubes and mixing grid have not been used in this study, neither in the *meshed zone* nor in the *extruded zones*. Such prismatic cells, which were cut into tetrahedrons for the use in TrioCFD (Angeli et al, 2015), improve indeed the resolution of wall boundary layers (Bieder et al, 2014). However, the complex geometry of dimples led to the formation of very small prismatic cells and thus to even smaller tetrahedrons. These small cells would drastically reduce the time step. Nevertheless, for further studies with heat transfer, it is planned to add two layers of prismatic cells to the fuel rods.

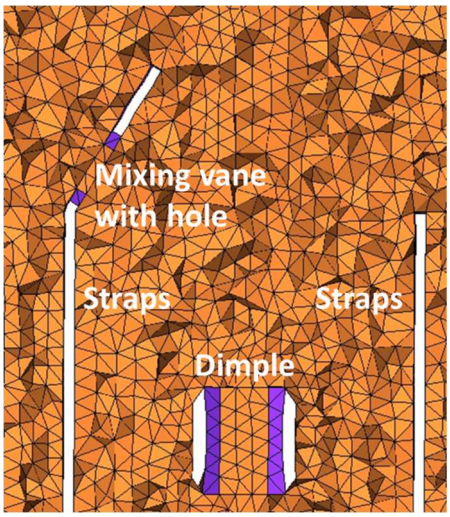


Fig.6 Meshing in the mixing grid with mixing vane and dimple

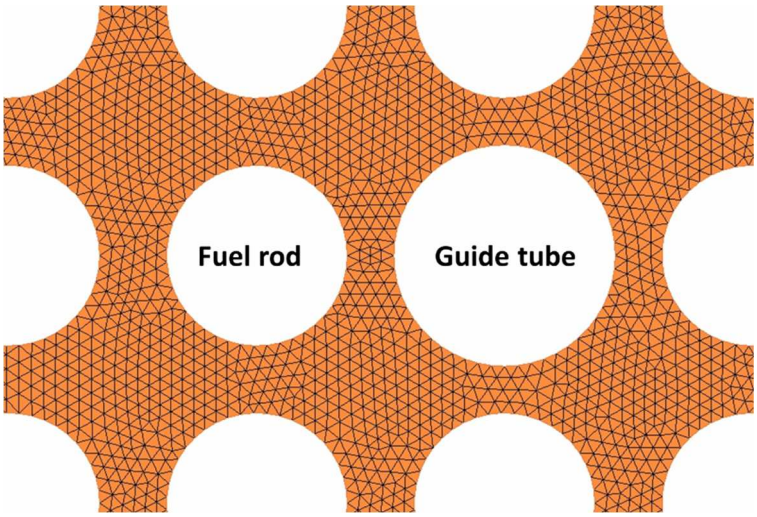


Fig.7 Meshing downstream of the mixing grid with fuel rods and a guide tube (control volumes for mass conservation)

The total mesh size of the complete calculation domain is about 130 million tetrahedrons for the fine mesh and 60 million tetrahedrons for the coarse mesh. As the velocity is discretized in the center of the faces of the tetrahedrons, the distance between two calculation points is about four times smaller than the reference size (about 0.25 mm for the fine mesh). Analogously, the number of velocity control volumes is twice as high as the number of tetrahedrons (260 million for the fine mesh). The fine mesh of a sub-channel is shown in Fig.8 where the control volumes of the velocity are visualized.

In order to put together clusters of various fuel assemblies of 17×17 rods, the meshing of the lateral faces of the assembly is periodic in x and y direction. Hence, clusters of 2×2 FAs or 1×3 FAs can be compounded easily.

Preliminary RANS calculations served to estimate a suitable mesh size for LES from the Taylor micro scale d_t, which is approximated according to:

$$d_t \approx \sqrt{10 \cdot \nu \cdot k/\epsilon}. \tag{16}$$

The Taylor micro scale defines the scale where the dominant dynamic forces of turbulence switch from inertial to viscous forces. A reasonable good meshing for LES should have a characteristic length that is close to this scale. The distribution of d_t in the assembly downstream of the grid is shown in Fig.8 for typical thermal hydraulic conditions in the reactor core (see chapter 5). In the central region of the sub-channel, d_t is in the order of 0.1 mm. The value descends to about 0.05 mm close to the walls of the rods (mean Kolmogorov scale ≈ 0.01 m). In the center of the sub-channels and in the grid region, the LES mesh approaches the characteristic length defined by the Taylor micro scale. Close to the walls, however, the flow might be under-resolved. This shortcoming is accepted in the actual phase of the study as Reichardt's wall law (eq.13) is applied to treat the near wall flow. It is important to note that the y^+ value on the rods is about 300 for the fine mesh.

Mesh convergence studies have been preformed for the RANS modelling approach with the coarse mesh and the fine mesh. The flow patterns within the *Meshed Zone* that were calculated with the coarse mesh differ from those calculated with the fine mesh. However, on the fine mesh, the RANS calculation lead in both *Meshed Zone* and downstream of the mixing grid to similar results as the temporal mean values of the LES. Hence, the RANS calculations were also realized on the fine mesh. Additional mesh refinement studies were not performed due to the resulting prohibitive high number of tetrahedrons.

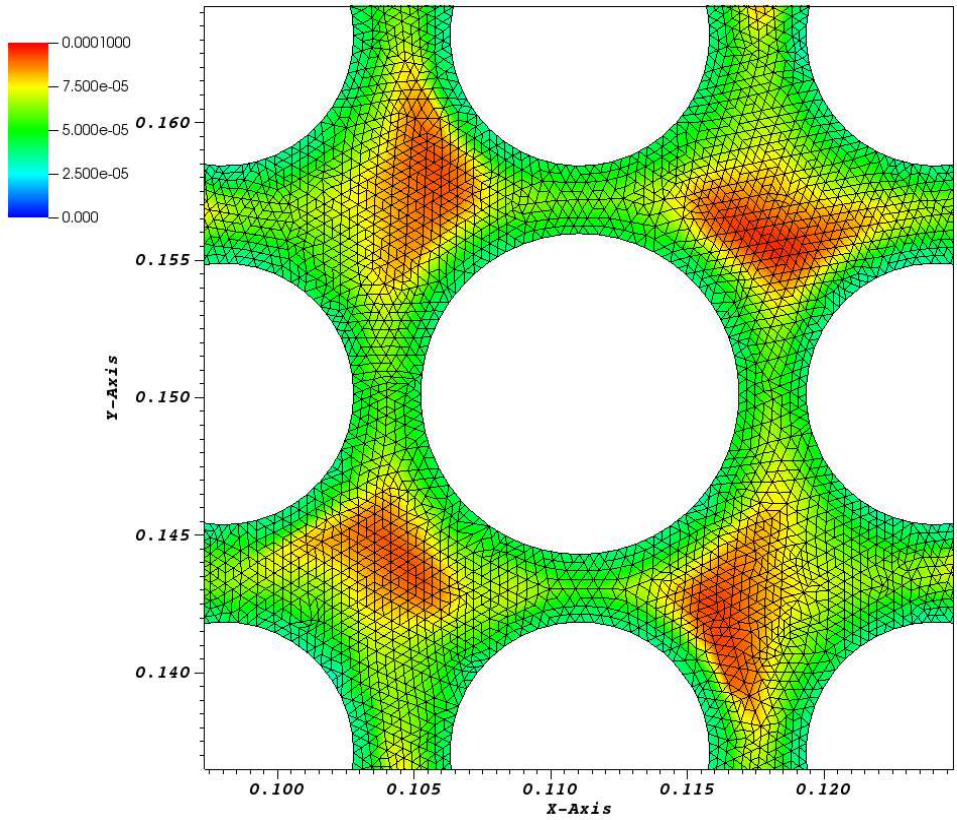


Fig.8 Distribution of the Taylor micro scale (in m) in the FA downstream of the grid and meshing of the control volumes of the velocity

3.5 VALIDATION OF THE NUMERICAL MODEL

The used approach is very close to that used in the analysis of four validation test cases that based on experiments: the IAEA rod bundle benchmark (Bieder et al. 2018), the AGATE experiments (Bieder et al., 2015 and Bieder et al., 2014) and the MATHYS_H experiments (Bieder, 2012). Numerical scheme of the validation cases, the meshing methods as well as the used sizes of the tetrahedral cells are very similar to the numerical approach, which is used in this study. Therefore, further validation is not discussed here. The presented numerical approach is considered as validated.

4. ANALYSIS OF THE MIXING IN FUEL ASSEMBLIES

Typical operating conditions at nominal power in a PWR core build the thermal hydraulic basis of this study. These typical conditions close to the core outlet are:

- Total pressure 16 MPa
- Mean coolant temperature 330 °C
- Mean coolant density 648 kg/m^3
- Dynamic viscosity 7.75×10^{-5} Pa s
- Mean coolant velocity 5.35 m/s
- Reynolds number 605,000

The physical properties are take constant.

4.1 ANALYSIS OF *INTRA-ASSEMBLY* MIXING

The main objective of this study is to provide a better insight into cross flow formation within a realistic fuel assembly of 17×17 fuel rods with mixing grid, known as *intra-assembly* flow. Although 260 million velocity control volumes are used, the turbulence modelling is insufficiently resolved near walls. By comparing the results of the two turbulence modelling approaches RANS and LES, the authors hope to derive a more robust interpretation of the results, especially due to the consideration of the unsteady flow behavior.

4.1.1 Results of the RANS calculation

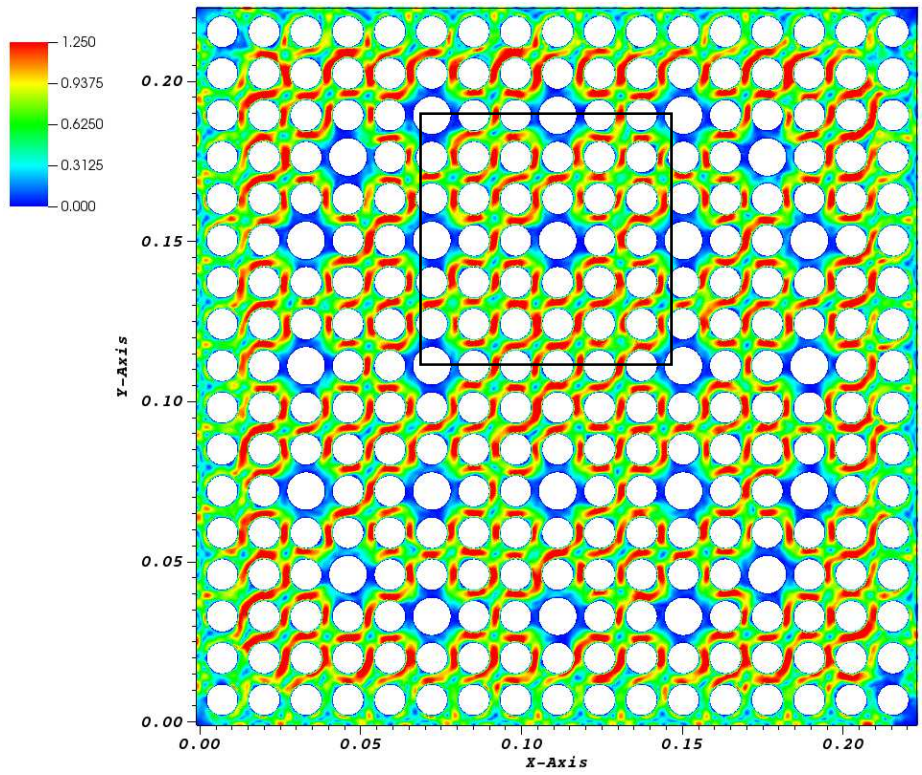
The norm of the cross flow velocity is defined as $|U_c| = \sqrt{{U_x}^2 + {U_y}^2}$. This cross flow is shown in Fig.9 in color scale for a horizontal plane at z=0.05 m, i.e. 0.05 m above the upper edge of the mixing grid lattice. In Fig.9a, the complete FA is shown. In Fig.9b a zoom around a guide tube is visualized and the flow direction is marked by the cross flow velocity vectors. The zoom region is marked in Fig.9a by the rectangle. According to the convention of numbering (n°=column:row), the guide tube has the number n°=9:12.

Form and orientation of the split type mixing vanes lead within the fuel assembly to the formation of extended cross flow along diagonal lines in +x, +y direction. The guide tubes, however, interrupt the diagonal flow patterns as can be seen in Fig.9b. The guide tubes have a larger diameter than the fuel rods and present thus an obstacle to cross flow. Furthermore, mixing vanes are not present in the sub channels around guide tubes (see Fig.3), what also hinders the formation of extended diagonal lines. Nevertheless, unhindered diagonal flow of short lengths develop near the assembly corners. The diagonals start at the rods with the numberings n°=13:1, 14:1 and 15:1 as well as n°=1:13, 1:14 and 1:15. Only six long diagonals of unhindered cross flow develop. These diagonals start at the rods with the numberings n°=3:1, 6:1 and 9:1 as well as n°=1:3, 1:6 and 1:9. These diagonals can be identified in Fig.9a and sections of four out of these six diagonals are visible in Fig.9b.

In the flow diagonals, which are broken by the presence of the guide tubes, closed circulation loops develop in the space between the guide tubes. Such circulation loops enclosing two fuel rods develop for example between the guide tube n° 9:12 and the neighboring guide tubes n° 6:9 and n° 12:15 (Fig.9b). The longest circulation loop develops across the central rod n° 9:9 that ranges from guide tube n° 6:6 to guide tube n° 12:12 (Fig.9a). Although the cross flow shown in Fig.9b seems to form closed circulation loops, the flow follows on its way in axial direction only a short distance on the loop since the cross flow velocity is much lower than the axial velocity.

The form of the cross flow diagonals change with increasing distance from the mixing grid. These modified patterns of the cross flow are shown in Fig.10 for a horizontal plane at z=0.15 m, i.e. 0.15 m above the upper edge of the mixing grid lattice. In Fig.10a shows the norm of the cross flow in the complete FA.

a)



b)

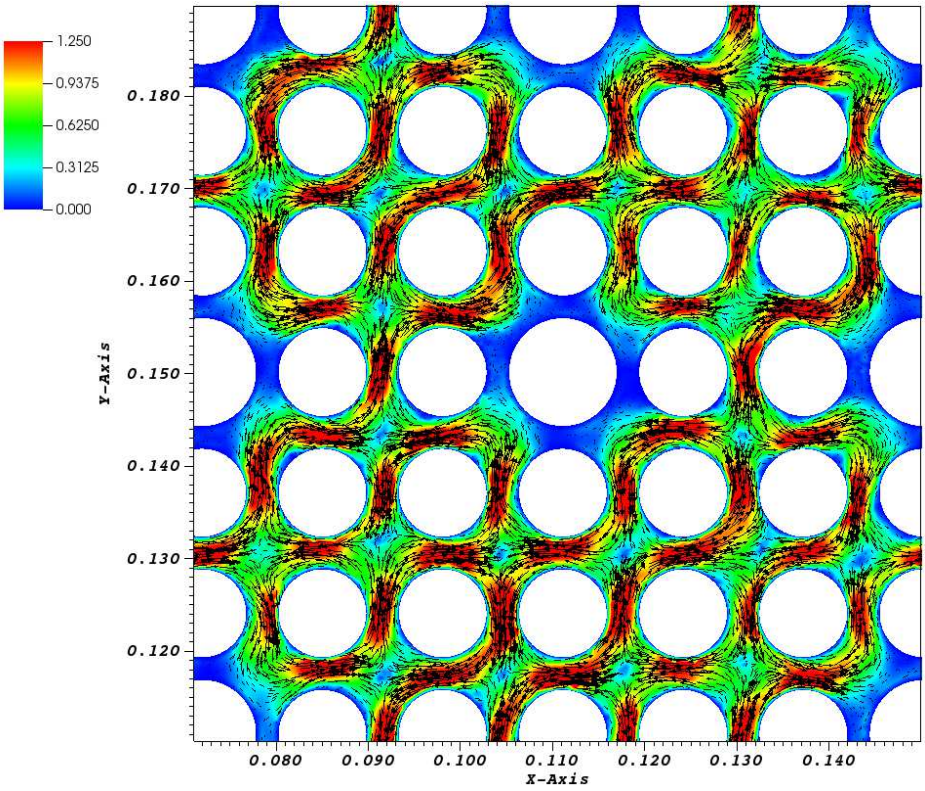
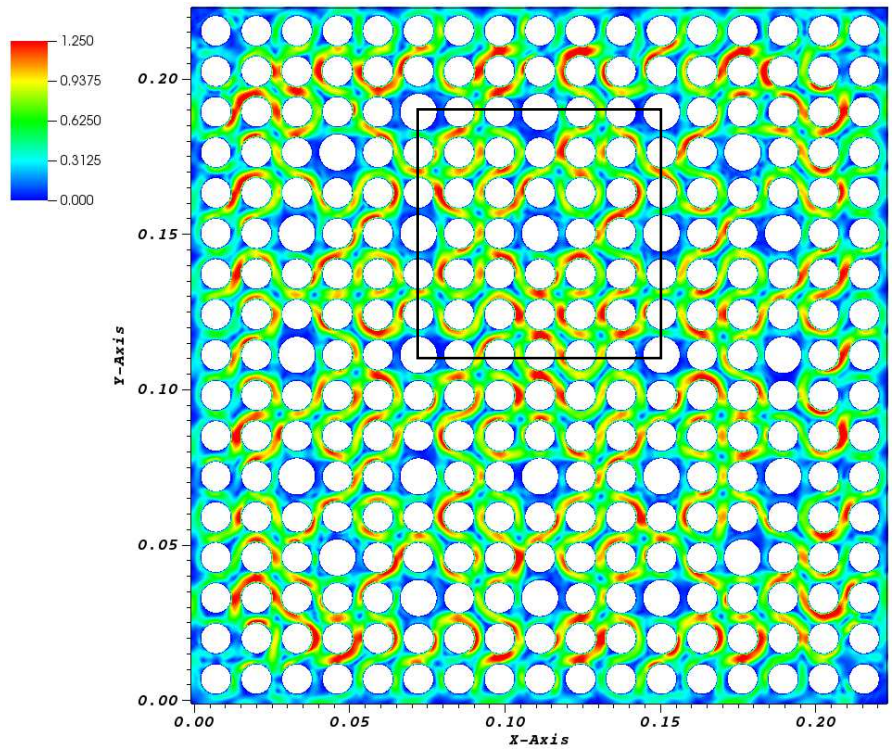


Fig.9 Norm of the cross velocity at z=0.05 m: a) complete FA and b) zoom to a guide tube (RANS)

a)



b)

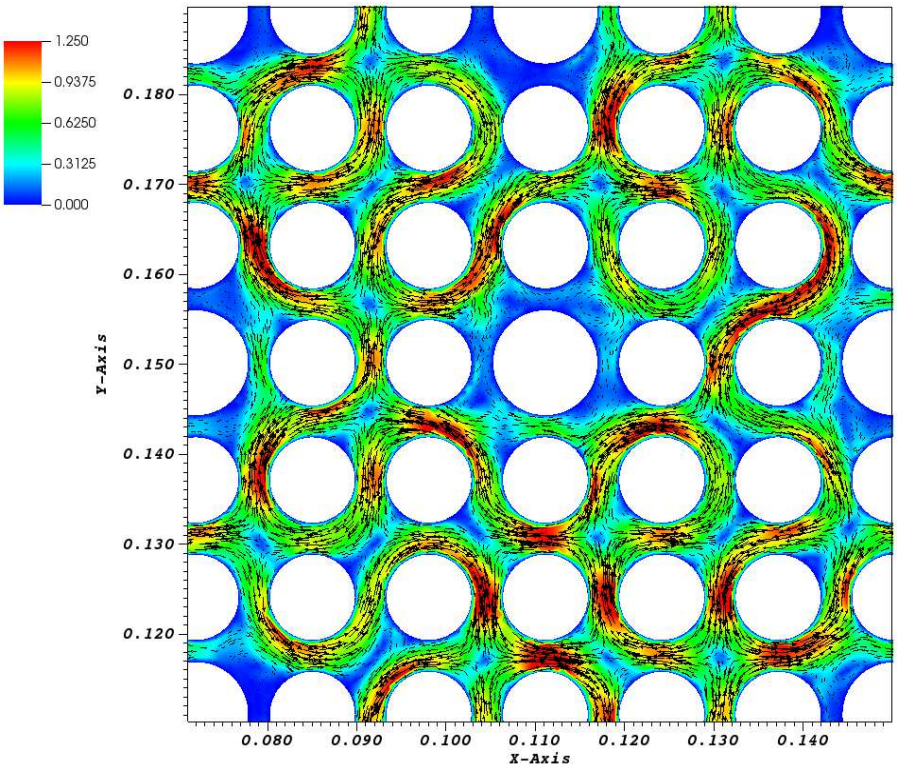


Fig.10 Norm of the cross velocity at z=0.15 m: a) complete FA and b) zoom to a guide tube (RANS)

In Fig.10b, the zoom around the guide tube number n°=9:12 is visualized and the flow direction is marked by the cross flow velocity arrows. The cross flow velocity is decreasing with increasing

distance from the grid. The long flow diagonals are still present, although they are disintegrating more and more with increasing distance from the mixing grid. The initial diagonal cross flow direction in +x, +y direction breaks up in separated streams in x-direction (e.g. between the rods 7:11 and 10:11) and y-direction (e.g. between the rods 11:10 and 11:14). Even an inversion of the diagonal flow direction in –x, +y direction is observed e.g. between the rods n° 10:10 and 6:14).

Such inversion of the flow direction has been detected in reduced scale experiments of rod bundles as the AGATE experiment (Bieder et al., 2014) and the NESTOR experiments (Kang and Hassan, 2015). Muller et al. (2017) have related such flow direction inversion to meta-stable solutions for the flow in rod bundles. The results presented here show that flow direction inversion cannot only exist in small scale experiments with a reduced number of rods (e.g. 5×5), but can also be present in realistic fuel assemblies of 17×17 rods.

4.1.2 Results of the LES calculation

Bieder et al, (2015) have shown that the use of linear eddy viscosity models as the k-ε model suppresses the formation of secondary flow structures, which are initiated in rod bundles by the formation of non-isotropic turbulence. Moreover, these models overestimate the stability of the diagonal cross flow. LES calculations were thus performed to confirm the results of RANS calculations. In analogy to Fig.9 (RANS), Fig.11 (LES) presents the cross flow for a horizontal plane at z=0.05 m. Mean values of the cross flow velocity ($|U_c| = \sqrt{\overline{u'_x}^2 + \overline{u'_y}^2}$) are shown that are averaged over 0.1 s. In this time period, the flow traverses approximately two times the calculation domain. In Fig.11a, the flow in the complete FA is shown and in Fig.9b a zoom around a guide tube is visualized, in which the cross flow velocity arrows mark the flow direction. The zoom region is marked in Fig.11a by the rectangle.

In the LES, the cross flow also arranges in diagonal direction. Both loop types are present: the long diagonals are shown in Fig.11a and the short recirculation loops are shown in Fig.11b. However, compared to the RANS calculation, the long diagonals are less clearly expressed and the shorter circulation loops are partly interrupted. Globally, the flow is more perturbed than in the RANS calculation. The time span to collect turbulence statistics might not be long enough to better homogenize the flow field. Low frequency fluctuations above 20 Hz are not resolved. Thus, to account for low frequency fluctuations, the analyzed time span must be significantly increased what is prohibitive due to the limited CPU power available. Fortunately, this aspect will not affect the main conclusions.

The form of the cross flow diagonals changes with increasing distance from the mixing grid. The cross flow velocity is decreasing at the same time. This is shown in Fig.12 for a horizontal plane at z=0.15 m. In Fig.12a, the norm of the cross flow velocity for the complete FA is shown, including the area of the domain zoomed in Fig.12b. In this figure, the cross flow velocity arrows mark the flow direction. As in the RANS calculation, the long flow diagonals are still present, although they are disintegrating more and more with increasing distance from the mixing grid. The initial diagonal cross flow direction in +x, +y direction breaks up in separated streams in x-direction and y-direction. However, the inversion of the diagonal flow direction in –x, +y direction is less obvious. A global reorganization of the flow is observed but the inversion of the flow direction is present only locally.

a)

b)

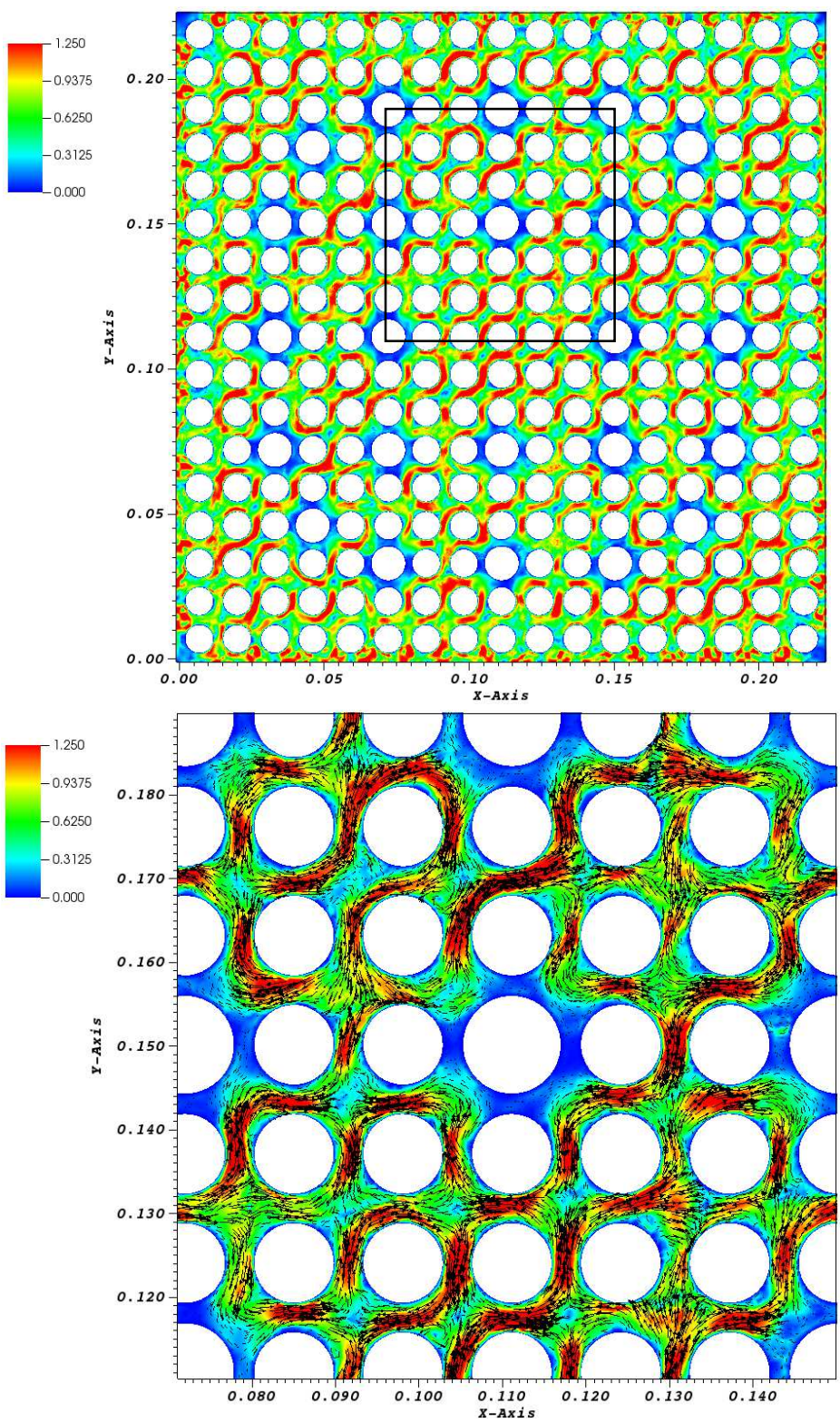


Fig.11 Norm of the cross velocity at z=0.05 m: a) complete FA and b) zoom to a guide tube (LES)

a)

b)

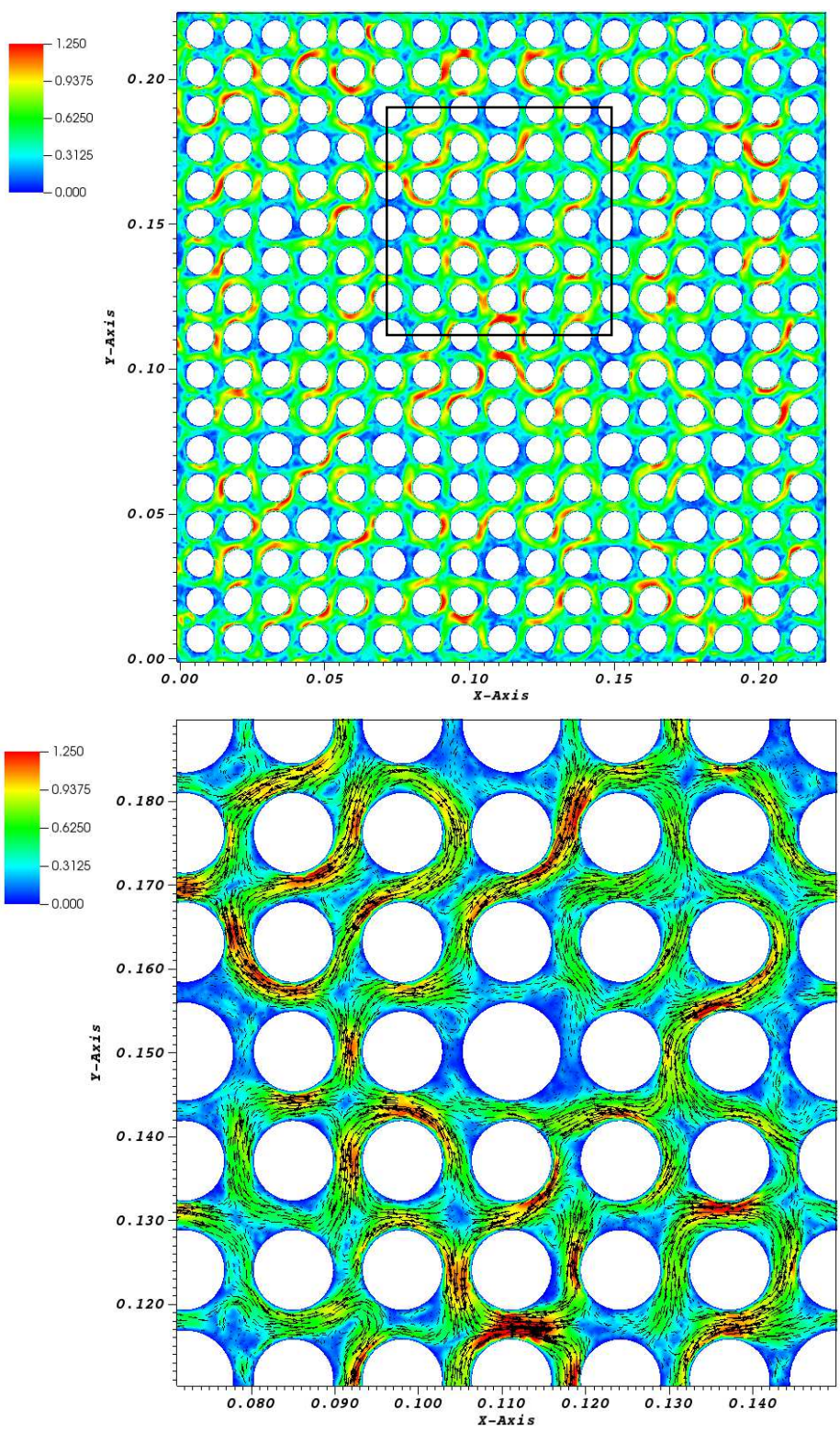


Fig.12 Norm of the cross velocity at z=0.15 m (LES): a) complete FA and b) zoom to a guide tube

Fig.13 shows the comparison of the flow field that was calculated for the real fuel assembly of 17×17 fuel rods to that of the AGATE experiment of 5×5 fuel rods. The LES result is presented. Bieder et al. (2014 and 2015) give more information on this CEA-experiment. A square sub-zone of 5×5 rods is defined in the center of the 17×17 rods assembly (central rod n° 9:9 and corner rods n° 7:7, 11:7, 7:11 and 11:11). The mean cross flow velocity for the horizontal planes at z=0.05 m and z=0.15 m is calculated in Fig.13 in analogy to Fig.11b (z=0.05 m), and Fig.12b (z=0.15 m). Temporal mean values are shown that are averaged over 0.1 s. These results are compared for similar hydraulic conditions

to the AGATE experiment (Re = 605,000 for the assembly calculation and Re = 95,000 for AGATE). The instantaneous cross flow velocity is averaged over 0.2 s. Close to the mixing grid at z=0.05 m, the cross flow diagonals develop similarly. Self-evidently, differences exist close to the walls of the housing of the AGATE experiments. Furthermore, in the experiment, the flow separates locally from the rods. This is not observed in the assembly calculation. Since the Reynolds number of the experiment is lower (Re=95,000), the near wall flow is better resolved in the experiment than in the whole assembly.

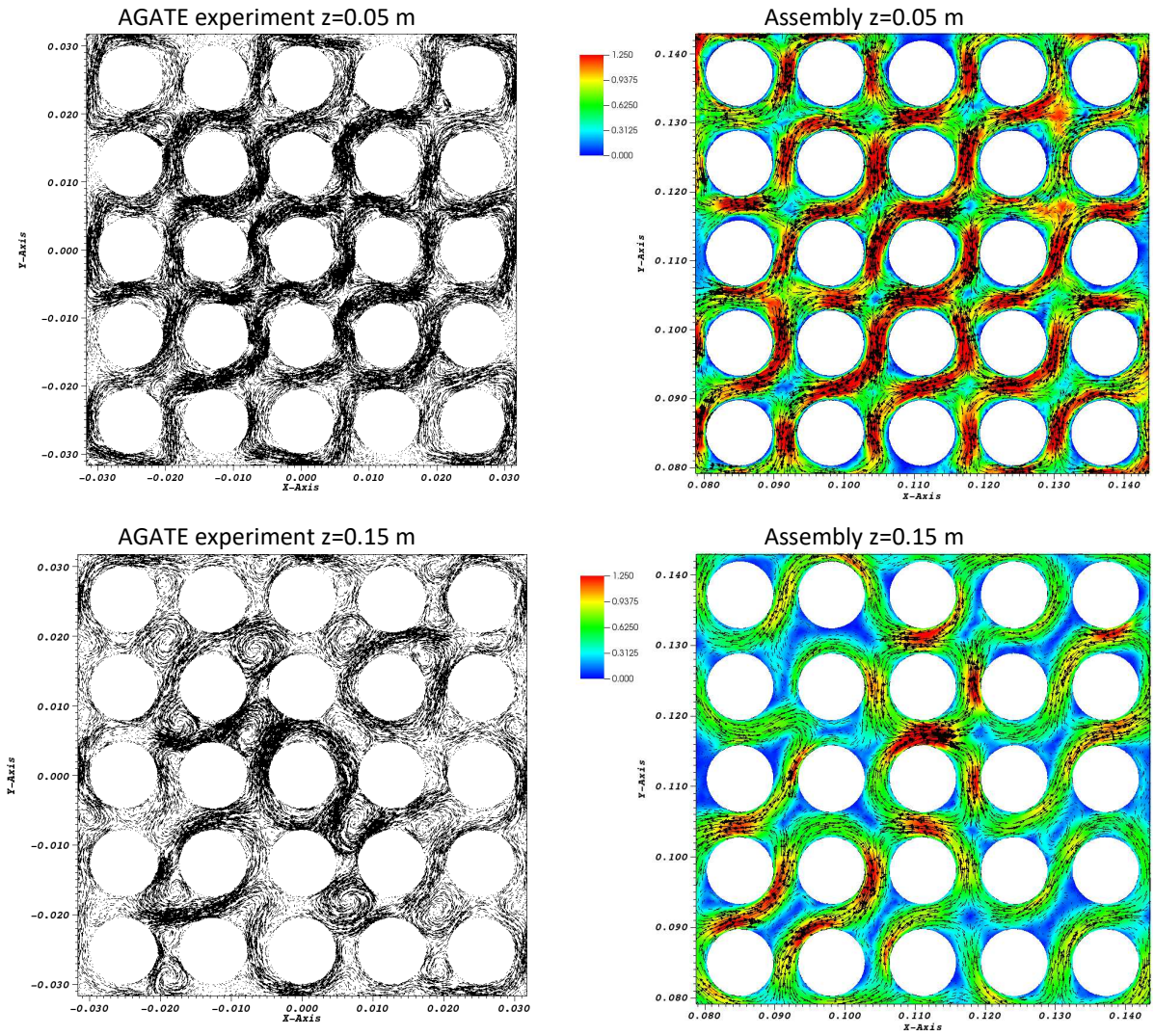


Fig.13 Cross flow in the AGATE experiment and in the center of the assembly (LES) at two distances from the mixing grid

Further downstream at z=0.15 m the flow patterns of the cross flow reorganize in both calculations, but develop differently in detail.

- In the AGATE experiment, the cross flow circulates in closed, circular loops around the central rod as well as around the two diagonally adjacent rods. This behavior is similar in the assembly calculation. Here, a closed flow loop encircles the central rod. The adjacent rods n° 8:8 and 10:10 are also encircled by the flow; however, the loops are not totally closed. The walls of the housing in AGATE might explain the closing of the loops.
- In the AGATE experiment, circular flow vortices develop in some sub-channels. Such vortices are not present in the assembly calculation (e.g. sub-channels below rods n° 8:9 and 8:10 and below rods n° 8:10 and 8:11). The velocity of the cross flow diagonals decreases slower in the assembly calculation than in AGATE and are still dominant at this distance from the grid.

It might be possible that the presence of the housing walls in the experiments significantly influence the reorganization of the flow in the wake of the grids. If intra fuel assembly mixing is assumed an important factor in the design of fuel assemblies, further investigations that are more detailed seem necessary to better understand the differences in the mixing behavior between fuel assembly experiments and fuel assemblies in the reactor core.

A macroscopic rotational flow within a FA was not detected. Thus, bulk mass fluxes across a certain row or column of fuel rods were not calculated. Such bulk fluxes are zero for an incompressible fluid and symmetry boundary conditions at the outer boundaries of the calculation domain due to mass conservation considerations.

4.2 ANALYSIS OF *INTER-ASSEMBLY* MIXING

The main objective of this study is to provide a better insight into the formation of cross flow between realistic fuel assemblies of 17×17 rods with mixing grids. This flow, which crosses the water gaps, is called *inter-assembly* flow. Four FAs, each of 17×17 rods, were gathered, forming a total calculation domain of 2×2 fuel assemblies. It is assumed that the water gap, i.e. the gap between two adjacent the FAs, has a width of 2 mm. Each 17×17 rods fuel assembly is identical to that of the study of the *intra-assembly* flow presented in chapter 4.1.

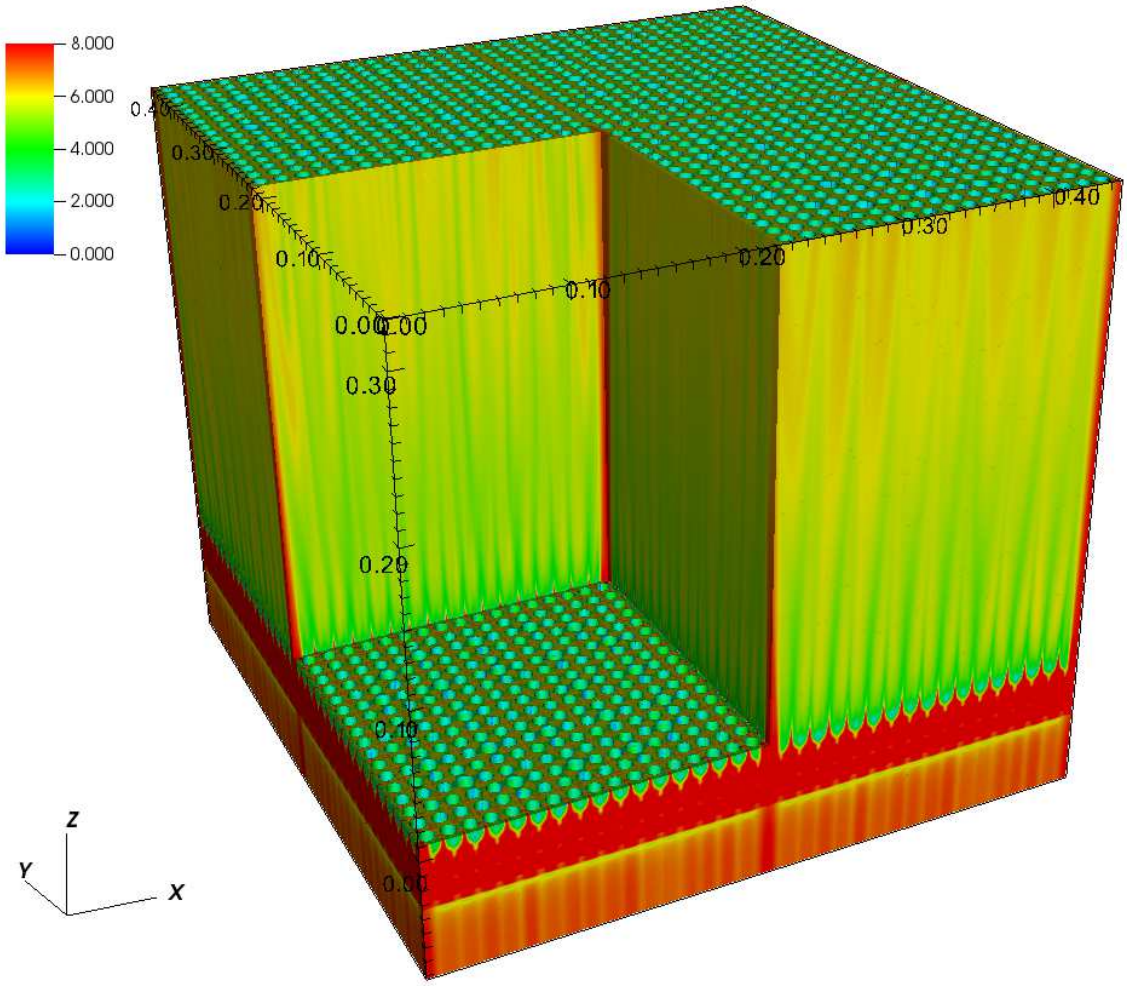


Fig.14 Time averaged value of the norm of the velocity ($|U| = \sqrt{\overline{u'_x}^2 + \overline{u'_y}^2 + \overline{u'_z}^2}$) in the complete calculation domain that is gathered by 2×2 fuel assemblies, each composed by 17×17 fuel rods. One FA is hidden for visualization purpose.

Since the meshing of each FA is identical and laterally periodic, the gathered 2×2 assemblies have conforming meshes. The complete calculation domain is shown schematically in Fig.14. For a better visualization, a part of one FA is hidden in the figure.

Concerning the *inter-assembly* flow, only the time-averaged results of the LES calculation are discussed. The turbulence statistics are calculated as explained in chapter 4.1.2. RANS calculations were realized but are not discussed here. As for the *intra-assembly* flow, these calculations support the conclusions.

The calculations were performed for the thermal hydraulic conditions of the *intra-assembly* flow study (Chapter 4.1). The time averaged value of the norm of the velocity ($|U| = \sqrt{\overline{u'}_x^{\,2} + \overline{u'}_y^{\,2} + \overline{u'}_z^{\,2}}$) is shown in Fig.14 in color scale. The whole calculation domain is represented. ¼ of the calculation domain is hidden for visualization purpose. Three flow features are noteworthy:

- The distribution of the velocity on the lateral front face at x > 0.224 m (middle of the water gap at y = -0.001 m) differs from that on the internal plane in the water gap at x < 0.224 m and y = 0.224 m. Hence, the *symmetry* boundary condition modifies the flow pattern in the lateral water gap.
- The flow significantly accelerates axially in the gap between the mixing grids. This acceleration occurs along the entire gap.
- The highest axial velocity develops in the central square sub channel that is formed by the four joining water gaps. Thus, the flow close to this central sub channel can be analyzed only with a calculation domain of 2×2 fuel assemblies.

The temporal mean of the norm of the velocity is shown in Fig.15 in color scale for a vertical plane at x = 0.1185 m. The plane is located in the center of the rod-to-rod gap, passing through a lattice strap of the mixing grid. The line in Fig.17 shows the location of this plane within the FAs.

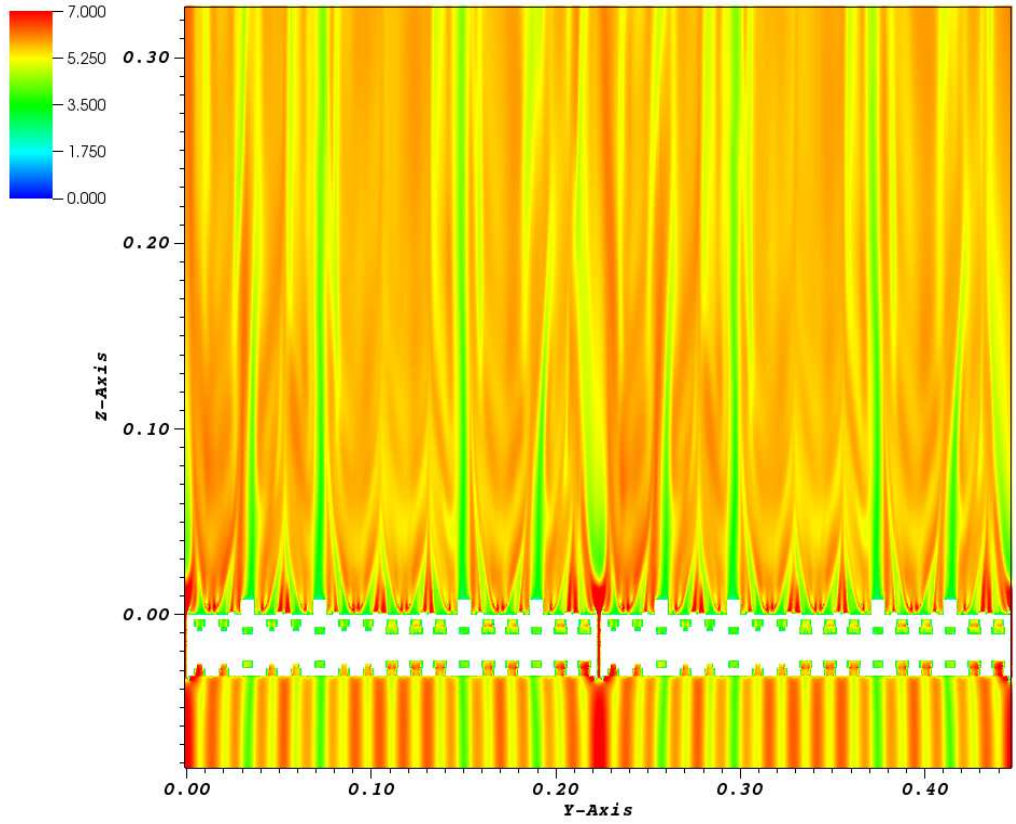


Fig.15 Norm of the velocity in the vertical plane at x=0.1185 m

The square vertical vanes (guide tube thimbles) that are located at the top of the lattice strap mark the location of the guide tubes of the control rods. Since guide tubes have larger diameters than fuel rods, the velocity in the guide tube-to-rod gaps is significantly reduced compared to the rod-to-rod gaps. The mixing vanes impose the cross flow as already discussed in chapter 4.1. The flow accelerates in the gap between the mixing grids. A notable fraction of fluid bypasses this gap by entering the neighboring rows of fuel rods. The velocity in the water gap is not distributed homogeneously in axial direction. The velocity decreases significantly in the wake of the protective tabs, which are oriented inside the assembly. These straps are placed equidistantly on the outer lattice straps.

The influence of the protective tabs on axial profiles of the norm of the mean velocity ($|U| = \sqrt{\overline{u'_x}^2 + \overline{u'_y}^2 + \overline{u'_z}^2}$) is shown in Fig.16 for two positions in the water gap: one between two fuel rods and one between two protective tabs. In the small figure included in Fig.16, dots mark these locations. Trapezes symbolize schematically the location of the protective tabs. The gray zone in Fig.16 indicates the location of the mixing grid. The velocity develops differently downstream of the grid lattice:

- Between the protective tabs, the flow keeps its high velocity of almost 8 m/s for an axial distance of about 0.015 m, before deaccelerating significantly. After reaching a minimum velocity of about 4 m/s at about z = 0.025 m, the flow accelerates again with increasing distance to the mixing grid.
- Between the rods, the flow first deaccelerates to about 3 m/s before accelerating to a similar value as for the flow profile located between the protective tabs.

These two profiles explain the presence of significant horizontal velocity gradients in the water gap.

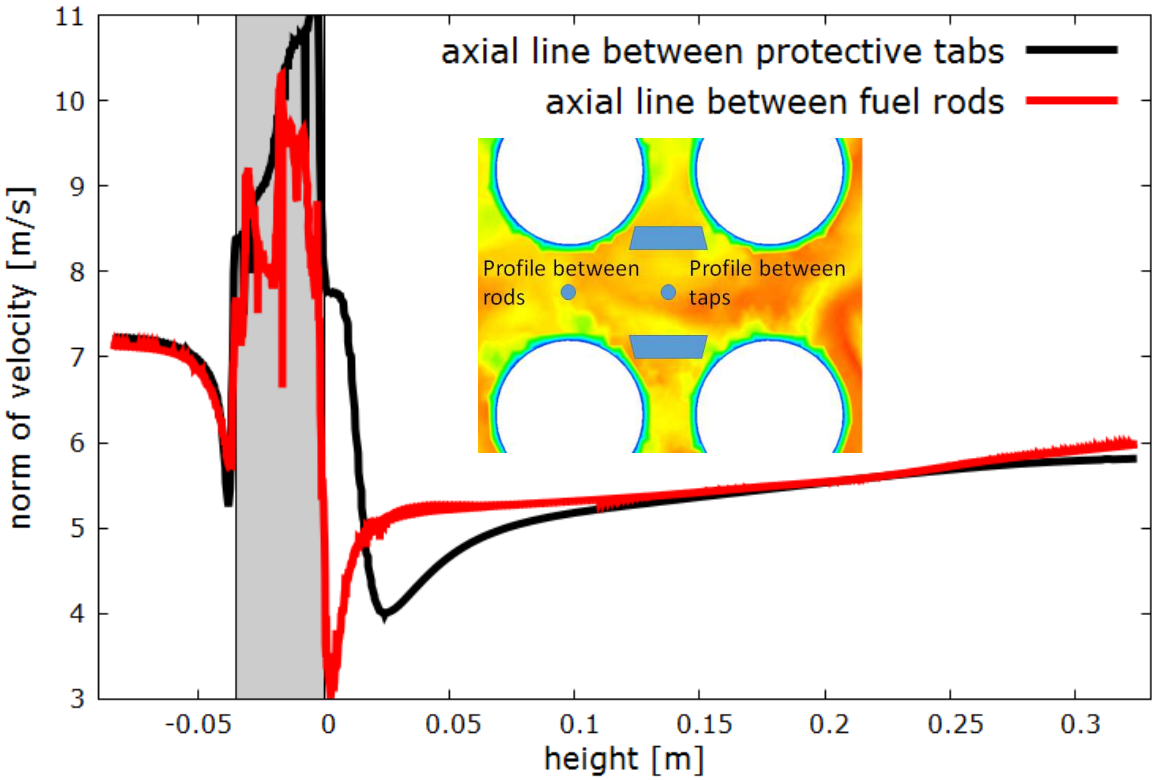


Fig.16 Axial course of the norm of the velocity in the gap between the assemblies at y=0.225 m for x=0.1185 m (sub channel gap) and x=0.113975 m (rod to rod gap)

The norm of the mean cross flow velocity ($|u_c| = \sqrt{\overline{u'_x}^2 + \overline{u'_y}^2}$) is shown in Fig.17 for a horizontal plane at z = 0.01 m, i.e. 0.01 m above the upper edge of the mixing grid lattice. The figure shows the

complete calculation domain of 2×2 FAs. The added line indicates the location of the vertical plane of Fig.15.

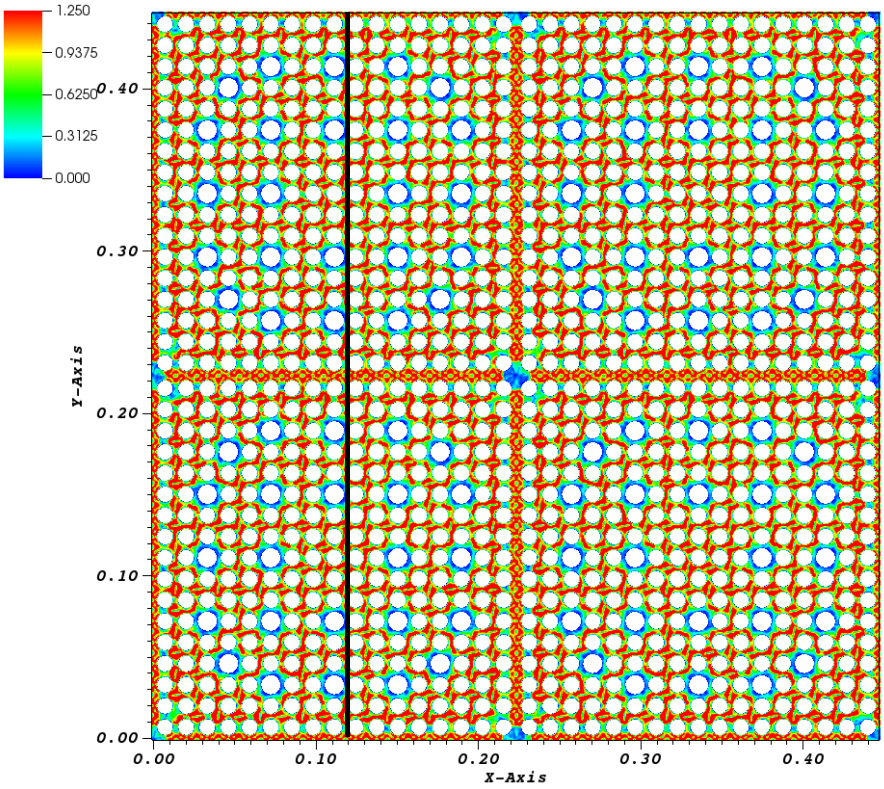


Fig.17 Norm of the temporal mean cross flow velocity ($|u_c| = \sqrt{\overline{u'}_x^{\,2} + \overline{u'}_y^{\,2}}$ in the horizontal plane at z = 0.01 m.

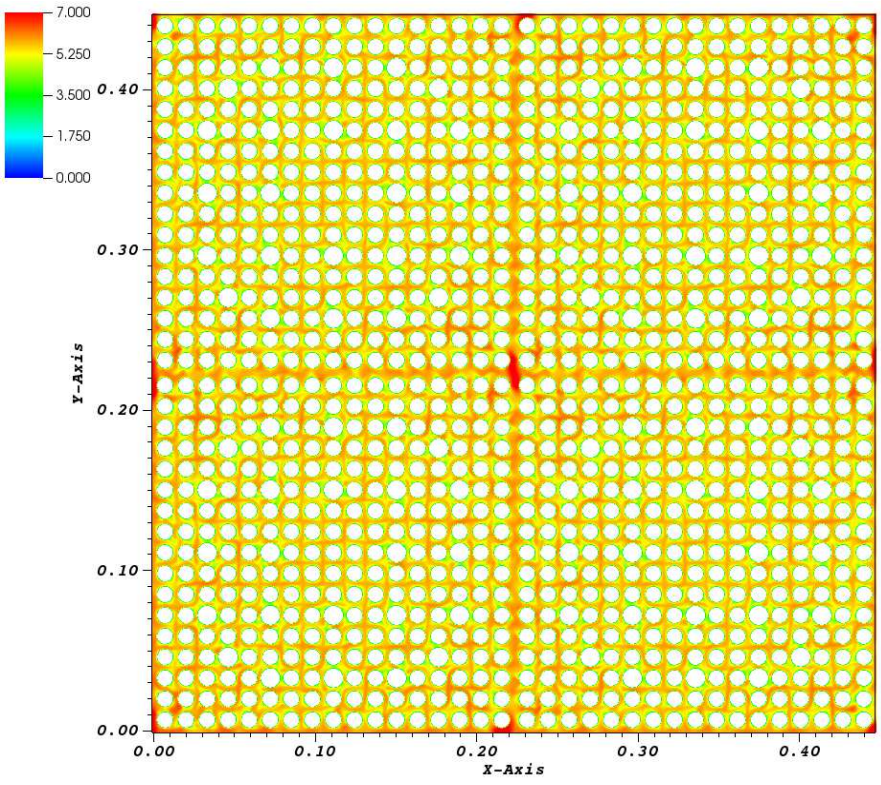


Fig.18 Norm of the temporal mean velocity $|U| = \sqrt{\overline{u'}_x^{\,2} + \overline{u'}_y^{\,2} + \overline{u'}_z^{\,2}}$ in the horizontal plane

at z = 0.25 m.

The mixing vanes initiate in each assembly the already discussed diagonal *intra-assembly* cross flow. The presence of the protective tabs leads to very complex swirling flow in the water gaps as discussed in Fig.16. Such swirls are not present in the central sub channel, which is formed at the intersection of four water gaps. The cross flow velocity is very small at this location.

The norm of the time averaged velocity $|U| = \sqrt{\overline{u'}_x^{\,2} + \overline{u'}_y^{\,2} + \overline{u'}_z^{\,2}}$ is shown in Fig.18 for a horizontal plane at z = 0.25 m, i.e. 0.25 m above the upper edge of the lattice of the mixing grid. The accelerated flow in the water gap as well as in the central sub channel is good visible. The horizontal distribution of accelerated and deaccelerated flow zones is very similar in each assembly. Only local differences in the flow distribution between the four FAs exist near the periphery of the calculation domain. The differences are introduced by the lateral “symmetry” boundary condition.

The mixing processes between fuel assemblies are analyzed in more detail close to the central sub channel which is located in the center of the complete 2×2 FA. Two distances from the mixing grid lattice are selected for the analysis of the norm of the mean cross flow velocity $|u_c| = \sqrt{\overline{u_x}^2 + \overline{u_y}^2}$, namely z = 0.05 m in Fig.19 and z = 0.25 m in Fig.20. Fig.19a shows the complete FA, Fig.19b shows a zoom to the central sub channel, which is formed by the intersection of four water gaps. In this figure, the velocity vectors of the cross flow norm mark the flow direction. The zoom region is marked in Fig.19a by the rectangle.

Form and orientation of the split type mixing vanes lead within each fuel assembly to the already discussed formation of extended cross flow along diagonal lines in +x, +y direction. However, as can be seen in Fig.19a, the water gaps interrupt the diagonal flow patterns. The interruption of the diagonals occurs along the whole water gap. Although, small scale vortices with complex shapes exist in the water gap, flow pattern with a significant cross wise velocity that can contribute to *inter-assembly* exchanges are not present close to the mixing grid (Fig.19b). Especially the central sub channel with its high axial velocity hinders efficient horizontal exchanges. Thus, close to the mixing grid, the water gaps act as barrier that efficiently holds back *inter-assembly* exchanges.

The isolation of the flow within each FA is even more clearly present further downstream of the mixing grid (Fig.20). *Intra-assembly* cross flow is clearly dominant over *inter-assembly* flow. The water gap separates the flow within neighboring assemblies from each other. Only the cross flow in the long diagonals, which is not hindered by the presence of control rod guide tubes, can traverse the water gaps in form of plane jets. The formation of these jets is visible in Fig.20b, each two rows above and below the central sub channel. From Fig.20a it is evident that these jets are extensions of the long diagonal *intra-assembly* cross flow across the water gaps. Again, the water gap act as barrier to *inter-assembly* exchanges.

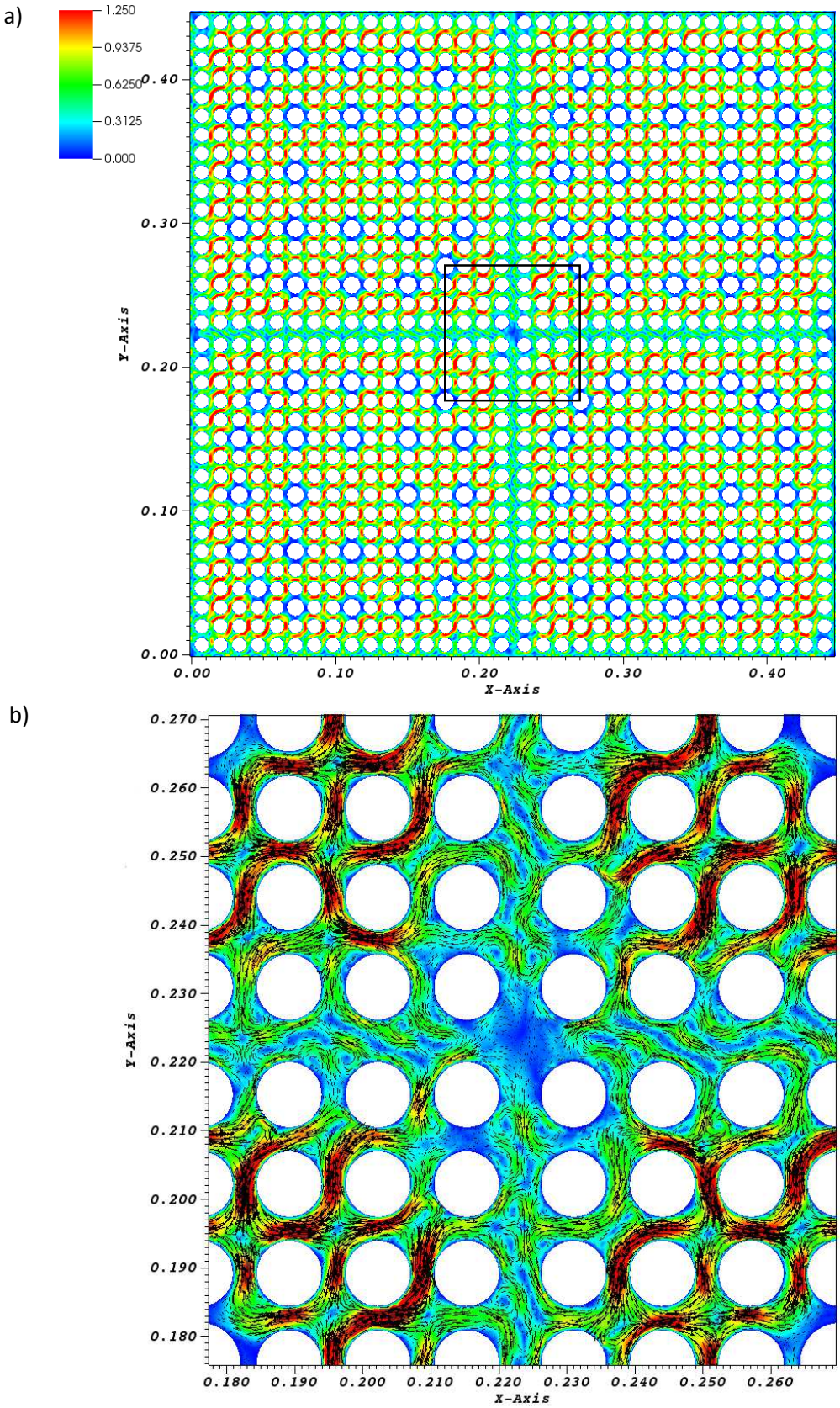


Fig.19 Norm of the time averaged cross flow velocity at z = 0.05 m: a) complete FA and b) zoom to the central sub channel

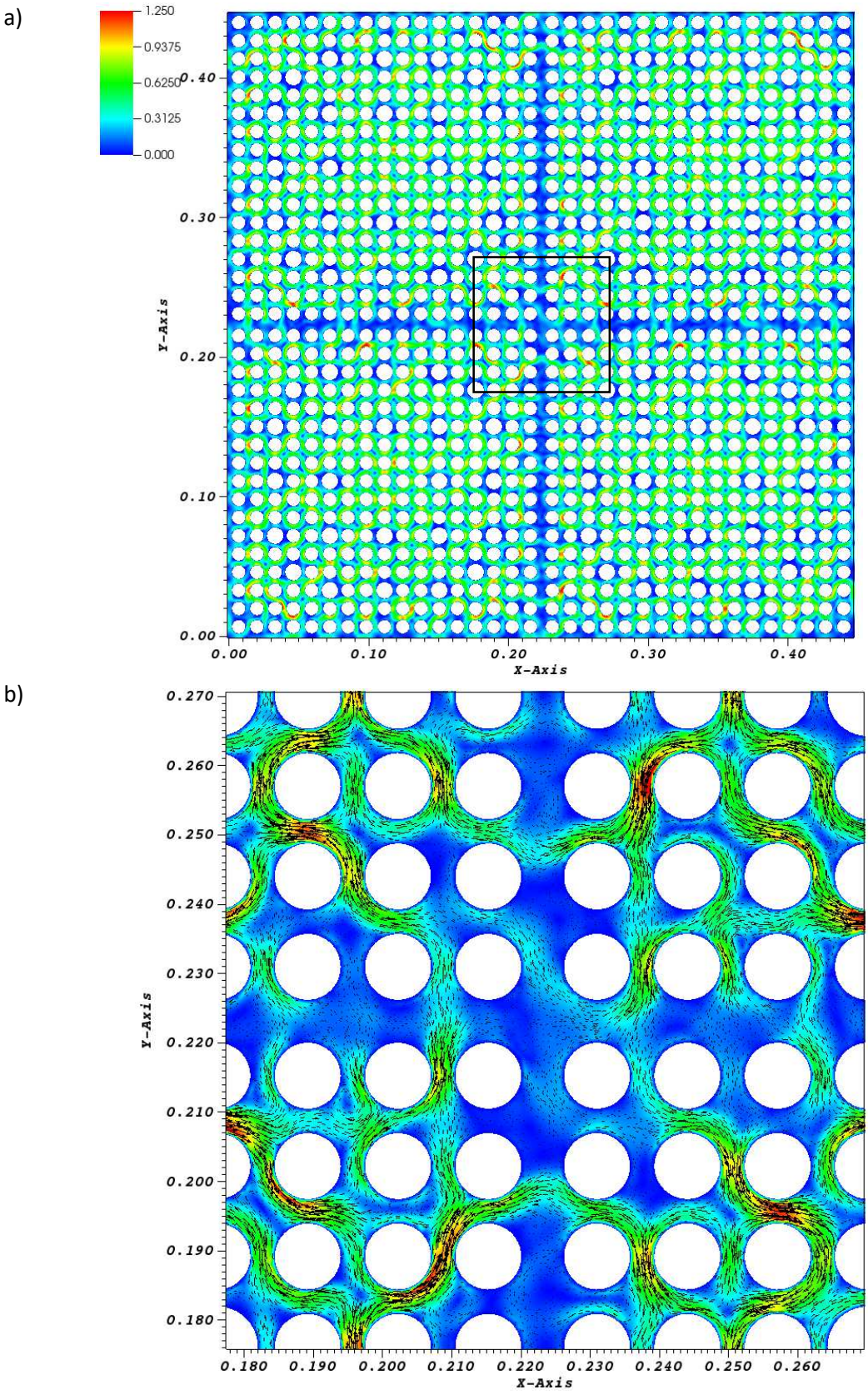


Fig.20 Norm of the time averaged cross flow velocity at z=0.25 m: a) complete FA and b) zoom to the central sub channel

In order to better visualize the *intra* and *inter-assembly* exchanges, a passive scalar tracer that has no influence on the flow field is injected in the 2×2 FA. The tracer is injected at the inlet plane with the concentration 1. Fig.21 shows the dispersion of the tracer in a horizontal plane at z = 0.25 m. Two injection zones are selected. The *intra-assembly* injection takes place in an area around the 9th column with 0.104 m < x < 0.118 m and -0.001 m < y < 0.447 m. The *inter-assembly* injection takes place along the water gap at 0.221 m < x < 0.225 m and -0.001 m < y < 0.447 m. For a better illustration, these injection domains are added to Fig.21 by the attached the small figure.

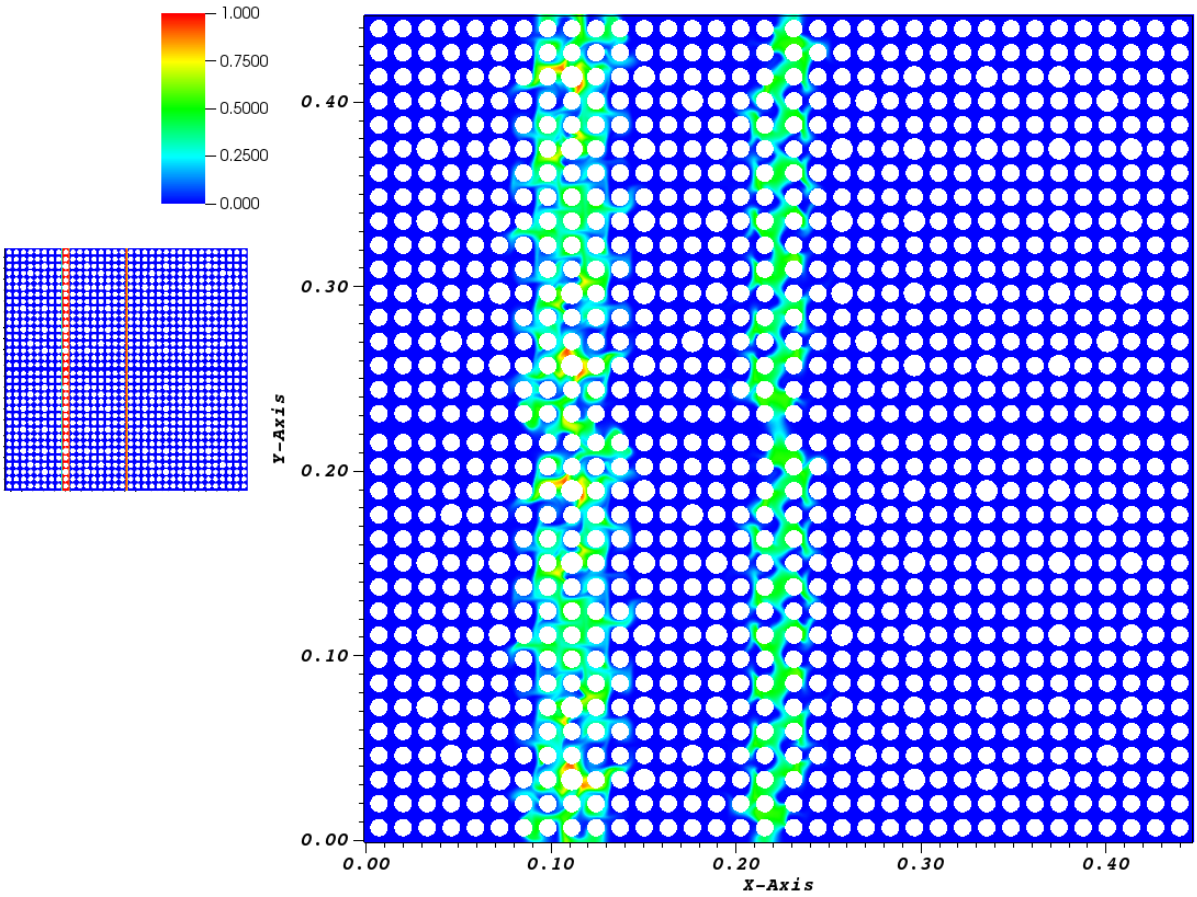


Fig.21 Dispersion of passive scalar injected in the inlet plane along column n°9 and the water gap

It is good visible that the *inter-assembly* exchanges across the water gap occur mainly in diagonal direction. This direction is imposed by the mixing vane orientation. In the last column of an assembly (column n°17 at x = 0215 m), one out of two mixing vanes in a row of fuel rods is directed towards the water gap. The interjacent mixing vanes are directed in parallel to the water gap in –y direction. Therefore, the diagonal flow is present only in one out of two rows. The horizontal dispersion of the tracer covers in each assembly approximately one column of fuel rods.

The *intra-assembly* exchanges are more irregular than the *inter-assembly* exchanges. Again, the diagonal flow direction is predominant. The most extended dispersion of the traces is located in the diagonals without the presence of control rod guide tubes. The most extended dispersion from column n°9 is located at distances of about 2.5 rows (row n° 6.5 and row n° 11.5). The presence of guide tubes reduce the influenced distance to about one row.

A macroscopic rotational flow interconnecting the four FAs was not detected. Thus, bulk mass fluxes across the water gaps were not calculated. These bulk fluxes are zero for an incompressible fluid and symmetry boundary conditions at the outer boundaries of the calculation domain due to mass conservation considerations.

4.3 COMPUTATIONAL TIME

All calculations have been performed on the Bull cluster "Occigen" of CINES[2], a supercomputer with a maximum power of 3.5 PFflop/s. 2800 processor cores of scalar Intel Xeon E5-2690-v4 processors were used for analyzing the flow in one FA. 8400 processor cores were used for analyzing the cluster of 2×2 FAs. The CPU time to reach convergence for the RANS cancelations as well as to collect the turbulence statistics for the LES calculations are given in Table 3.

Table 3: CPU time in h to reach convergence and to collect turbulence statistics

	1 assembly		**2×2 assembly**		**Machine time**
Turbulence model	M tetras	Cpu hours 2800 cores	M tétras	Cpu hours 8400 cores	
RANS	130	64,000	520	250,000	About 1 day
LES	130	320,000	520	1,300,000	About 5 days

The almost linear relationship between CPU times, mesh numbers and processor cores shows the good parallel performance of TrioCFD under realistic production conditions.

[2] CINES: Centre Informatique National de l'Enseignement Supérieur. https://www.cines.fr/

5. CONCLUSION

The flow within and between full cross-section fuel assemblies with generic but realistic mixing grids have been analyzed by CFD using high performance computing (HPC). The analyzed assembly consists of a bundle of 17×17 rods including fuel rods, control rod guide tubes and a mixing grid with split type mixing vanes. The axial length of the analyzed domain spans approximately the distance between two consecutive mixing grids. *Intra-assembly* flow is analyzed by modelling one single assembly; *inter-assembly* flow is analyzed by modelling a bundle of 2×2 fuel assemblies, each with 17×17 rods and a mixing grid. Only hydraulic effects of the mixing grids on the behavior of the flow are analyzed, power input and heat transfer are not considered.

The numerical model has already been validated by comparing calculation results to MATHIS_H and AGATE experiments. After further numerical tests and mesh refinement studies, both tested turbulence modelling approaches, namely RANS modelling with the standard k-ε model and statistically converged LES with the WALE model, lead to similar flow fields. Thus, both turbulence models support the same conclusions concerning the formation of cross flow.

Concerning the *intra-assembly* flow, it was shown that control rod guide tubes, which have a larger diameter than fuel rods, significantly hinder the formation of cross flow. Especially the formation of extended diagonal flow lines were suppressed, which are initiated by split type mixing vanes. Reduces scale experiments with 5×5 rods might represent the flow field in the center of an assembly. Inversion of the diagonal flow direction as detected in reduced scale experiments might also happen in full-scale fuel assemblies.

Concerning the *inter-assembly* flow, it was shown that the water gap could act as a flow barrier between neighboring fuel assemblies. The main exchanges across the water gap occurs in extension of the long flow diagonals that develop within an assembly. Generally, the *intra-assembly* exchanges are more efficient than *inter-assembly* exchanges.

As perspective, a more profound comparison of full cross-section assembly calculations to experiments and to more detailed LES are planned, both based on the AGATE experiments. Further, heat transfer will be considered as well as the influence of deformed fuel assemblies on *intra* and *inter* assembly mixing.

Acknowledgement

This work was granted access to the HPC resources of CINES under the allocation A0052A07571 made by GENCI.

References

Agbodemegbe V., Cheng X., Akaho E. and Allotey F., 2015. Correlation for cross-flow resistance coefficient using STAR-CCM+ simulation data for flow of water through rod bundle supported by spacer grid with split-type mixing vane. Nucl. Eng. Des., 285, 134-149.

P.-E. Angeli, U. Bieder U., G. Fauchet, 2015 Overview of the Trio_U code: Main features, V&V procedures and typical applications to engineering, 16th International Topical Meeting on Nuclear Reactor Thermal Hydraulics, NURETH-16, Chicago, USA (2015)

P.-E. Angeli, M.-A. Puscas, G. Fauchet and A. Cartalade: FVCA8 Benchmark for the Stokes and Navier–Stokes Equations with the TrioCFD Code—Benchmark Session. In: Finite Volumes for Complex Applications VIII - Methods and Theoretical Aspects, pp.181-202 (2018)

Bieder U., Costa D.: Analysis of the Heat Transfer in a 4x4 Rod Bundle. Annals of Nuclear Energy 115 (2018) 352–366

Bieder U., F. Falk, G. Fauchet: CFD analysis of the flow in the near wake of a generic PWR mixing grid, Ann. Nucl. Energy (2015)

Bieder U., F. Falk, G. Fauchet: LES analysis of the flow in a simplified PWR assembly with mixing Grid, Progress in Nuclear Energy 75 (2014) 15-24

Bieder U.: Analysis of the flow down- and upwind of split-type mixing vanes. OCDE workshop CFD4NRS-4, Daejeon, Corée de Sud, 10-12 September 2012

Capone L., 2012. CFD ANALYSIS OF NUCLEAR FUEL BUNDLES AND SPACER GRIDS FOR PWR REACTORS. PhD Thesis, Texas A&M University

Capone L., Hassan Y. and Benhamadouche S., 2013. Large eddy simulation for 5×5 MATHIS_H fuel bundle configuration using the split vanes with Code_Saturne. 15th International Topical Meeting on Nuclear Reactor Thermal Hydraulics, NURETH-15, Pisa, Italy.

Conner M., Hassan Y. and Dominguez-Ontiveros E., 2013. Hydraulic benchmark data for PWR mixing vane grid. Nuclear Engineering and Design, 264, 97-102.

Delafontaine S., Ricciardi G., 2012. Fluctuating pressure calculation induced by axial flow trough mixing grid. Nuclear Engineering and Design, 242, 233 – 246.

Delafontaine S., 2018. Simulation of unsteady fluid forces on a single rod downstream of mixing grid cell. Nuclear Engineering and Design 332, 38–58

Ducros F., Bieder U., Cioni O., Fortin T., Fournier B.,Fauchet G., Quéméré P., 2010., Verification and validation considerations regarding the qualification of numerical schemes for LES for dilution problems. Nuclear Engineering and Design, 240, 2123-2130.

Fortin T., 2006. Une méthode d'éléments finis à décomposition L2 d'ordre élevé motivée par la simulation des écoulements diphasiques bas Mach. PhD thesis, Université Paris VI

Gandhir A. and Hassan Y., 2011. RANS modeling for flow in nuclear fuel bundle in pressurized water reactors. Nuclear Engineering and Design, 241, 4404-4408.

Guermond J.L., Quartapelle L., 1998. On the Stability and Convergence of Projection Methods Based on Pressure Poisson Equation. International Journal of Numerical Methods in Fluids 26, 1039–1053

Hirt C.V., Nichols B.D., Romero N.C., 1975. SOLA - A numerical solution algorithm for transient flow. Los Alamos National Lab., Report LA-5852.

Höhne, TH, Kliem, S., Bieder, U., 2006. Numerical modelling of a buoyancy-driven flow experiment at the ROCOM test facility using the CFD codes CFX and Trio_U, Nuclear Engineering and Design, 236 (12), pp 1309-1325, 2006

Holloway M., Beasley D. and Conner M., 2008. Single-phase convective heat transfer in rod bundles. . Nuclear Engineering and Design, 238, 848-858.

Ikeno T., T.Kajishima, T.Mutara, 2006. The Effect of Mixing-vane Arrangements in a Sub-channel Turbulent Flow. Journal of Nuclear Science and Technology, Volume 43, Issue 10

Kang S. and Hassan Y., 2016. Computational fluid dynamics (CFD) round robin benchmark for a pressurized water reactor (PWR) rod bundle. Nuclear Engineering and Design 301, 204–231

Karoutas Z., Gu C.-Y., and Schölin B., 1995. 3-D flow analyses for design of nuclear fuel spacers. 7th International Topical Meeting on Nuclear Reactor Thermal Hydraulics, NURETH-7, Saratoga Springs, USA

Kuzmin D., Turek S., 2004. High-resolution FEM-TVD schemes based on a fully multidimensional flux limit. Journal of Computational Physics 198, 131–158

Li X. and Gao Y., 2014. Methods of simulating large-scale rod bundle and application to a 17×17 fuel assembly with mixing vane spacer grid. Nucl. Eng. Des., 267, 10-22.

Mikuž B. and F. Roelofs, 2018. Low resolution modelling of mixing phenomena in PWR fuel assembly with split type mixing grid. International Seminar on Nuclear Reactor Core Thermal Hydraulics Analysis, IS-ReCTHA, Lecco, 29-31 August

Mikuž B. and Tiselj, I., 2017. URANS prediction of flow fluctuations in rod bundle with split-type spacer grid. Int. J. Heat Fluid Flow, 64, 10-22.

Muller F., Gréa B.J., Burbeau A., Sageaut P., 2017, Minimum enstrophy states and bifurcations in 2D Euler flows around a central obstacle. 23ème Congrès Français de Mécanique, Lille, 28 September

Navarro M. and Santos A. A., 2011. Evaluation of a numeric procedure for flow simulation of a 5×5 PWR rod bundle with a mixing vane spacer. Prog. Nucl. Energy, 53, 1190-1196.

Nguyen T. and Hassan, Y., 2017. Stereoscopic particle image velocimetry measurements of flow in a rod bundle with a spacer grid and mixing vanes at a low Reynolds number. Int. J. Heat Fluid Flow 67, 202-219.

A. Rashkovan, D. McClure, D. R. Novog, 2014. Examination of Separate-Effect and Integral Phenomena Within a Grid Spacer with Mixing Vanes: Results for the MATiS-H OECD_NEA Benchmark Exercise. Nuclear Science and Engineering, 177, 141-155

H. Reichardt. Vollständige Darstelling der turbulenten Geschwindigkeitsverteilung in glatten Leitungen. Zeitschrift für Angewandte Mathematik und Mechanik, Vol 31, p 208, 1951

Smith B., Song C.-H., Chang S.-K., Lee J. and Kim J., 2013. Report of the OECD/NEA KAERI rod bundle CFD benchmark exercise. Paris, France: NEA/CSNI (2013)5.

W.B. Weihermiller, G.S. Allison, LWR NUCLEAR FUEL BUNDLE DATA FOR USE IN FUEL BUNDLE HANDLING, Batelle Topical Report, US Department of Energy, Spent Fuel Project Office, Contract EY-76-C-06-1830, 1979

J. Yan, Y. Zhang, B. Yang, W. Li, and Y. Zhou, 2014. “Influence of Spacer Grid Outer Strap on Fuel Assembly Thermal Hydraulic Performance” Science and Technology of Nuclear Installations, Volume 2014, Article ID 602062,

A. T. Ylönen, 2013. High-resolution flow structure measurements in a rod bundle. Dissertation ETH Zürich, DISS. ETH No. 20961